

1 Bayesian paleomagnetic Euler pole inversion for 2 paleogeographic reconstruction and analysis

3 Ian R. Rose¹, Yiming Zhang¹, and Nicholas L. Swanson-Hysell¹

4 ¹Department of Earth and Planetary Science, University of California, Berkeley, CA, USA

5 **Key Points:**

- 6 Paleomagnetic Euler pole analysis can be implemented as a Bayesian inverse problem
7 that incorporates uncertainty on pole positions and ages
- 8 This approach provides estimates of absolute plate rates with uncertainties and
9 can solve for the timing of Euler pole changepoints
- 10 Applying this method to Australia paleomagnetic data yields plate motions that
11 are consistent with those from independent plate models

Corresponding author: Nicholas L. Swanson-Hysell, swanson-hysell@berkeley.edu

Abstract

Apparent polar wander paths (APWPs) synthesized from paleomagnetic poles provide the most direct data for reconstructing past paleogeography and plate motions for times earlier than ca. 200 Ma. In this contribution, we describe a new method for APWP synthesis that extends the paleomagnetic Euler pole analysis of Gordon et al. (1984) by placing it within the framework of a Bayesian inverse problem. This approach incorporates uncertainties in pole positions and age that are often ignored in standard treatments. The paleomagnetic Euler poles resulting from the inversions provide estimates for full-vector plate motion (both latitude and longitude) and associated uncertainty. The method allows for inverting for one or more Euler poles with the timing of changepoints being solved as part of the inversion. In addition, the method allows the incorporation of true polar wander rotations, thus providing an avenue for probabilistic partitioning of plate tectonic motion and true polar wander based on paleomagnetic poles. We show example inversions on synthetic data to demonstrate the method's capabilities. We illustrate application of the method to Cenozoic Australia paleomagnetic poles which can be compared to independent plate reconstructions. A two-Euler pole inversion for the Australian record recovers northward acceleration of Australia in the Eocene with rates that are consistent with plate reconstructions. We also apply the method to constrain rapid rates of motion for cratonic North America associated with the Keweenawan Track of late Mesoproterozoic paleomagnetic poles. The application of Markov chain Monte Carlo methods to estimate paleomagnetic Euler poles can open new directions in quantitative paleogeography.

Plain Language Summary

Movement of Earth's tectonic plates results in large changes in continent positions over time known as paleogeography. Reconstructing paleogeography is central for understanding long term changes to Earth's surface and interior. Ocean floor data are very useful for determining these motions, but only exist for the most recent 4% of Earth's history. For older times, we use magnetic directions in rocks that show positions relative to the north pole. These records are called paleomagnetic poles and plate motions result in progressions of paleomagnetic poles called paths. Earth scientists need ways to synthesize poles into paths. Ideally, such a synthesis uses uncertainties on pole positions and ages. We developed a new way to reconstruct plate motion from paleomagnetic poles using an approach called Bayesian inversion. We apply the method to pretend data to illustrate its capabilities. We then apply the method to real data such as that from Australia over the past 60 million years. This analysis shows change in the continent's position and the rate of its motion that is similar to approaches that rely on ocean floor data. For older times, the method can help reconstruct positions and provide estimates of plate motion rates and associated uncertainty.

Introduction

Plate tectonics is the differential motion of near-rigid blocks of lithosphere across the surface of Earth, separated by relatively narrow regions of deformation in spreading centers, transform faults, and subduction zones. The relative rigidity of plates means that the motion of most of Earth's surface can be described by a set of Euler poles which specify the position (in latitude and longitude) of a rotation axis and a rate of rotation about this axis for a given plate (cf. Cox & Hart, 2009). Individual points on a plate undergoing rigid rotation are described by small circle paths (Fig. 1).

Euler poles are widely used for describing plate motions due to their simplicity and compactness (e.g. DeMets et al., 2010; Argus et al., 2011). Motion between tectonic plates has a tendency to remain constant, or approximately so, over time scales of millions of years (e.g. Iaffaldano et al., 2012; Müller et al., 2016). This consistency of motion can

be seen physically expressed in the shape of oceanic fracture zones and in hotspot tracks across the lithosphere. These features often form gently curving arcs over large portions of Earth's surface that can be well described by small circles, consistent with finite Euler rotations of the plate for an extended period of time. As such, the combination of an Euler pole plus a time interval for which it is active (often called a "stage pole") is a convenient description of plate motions through Earth history.

The stage pole description of plate motions has been widely used in both continental reconstructions (e.g. Boyden et al., 2011) and in geodynamical modeling (e.g. McNamara & Zhong, 2005; Bull et al., 2014). Most reconstructions of plate motions over the past 200 million years rely heavily on fitting Euler pole rotations to oceanic fracture zones, hotspot tracks, seafloor magnetic isochrons, and, to a lesser extent, paleomagnetic data (Müller et al., 1993; Seton et al., 2012; Müller et al., 2016). These relative plate motions are used to construct plate circuits that relate plates to one another and to the spin axis (e.g. Müller et al., 2016; Torsvik & Cocks, 2017). However, as we look further back in Earth history, many of the records on which these plate tectonic reconstructions rely largely disappear due to the subduction of oceanic lithosphere. Given the lack of oceanic crust older than ~ 200 Ma, the paleomagnetic record from continental rocks is the dominant remaining data. These paleomagnetic data can be used in conjunction with geological data that provides information on the tectonic setting of continental margins as well as additional information, such as the correlation of geologic terranes, to develop paleogeographic reconstructions.

It is more challenging to reconstruct past plate motions from paleomagnetic pole positions than from data derived from oceanic lithosphere for a number of reasons, including: (1) the data are often sparser; (2) traditional paleomagnetic analysis constrains paleolatitude and the orientation of a continental block, but does not constrain paleolongitude without additional assumptions; and (3) paleomagnetic poles can have appreciable uncertainty in both position and age.

Gordon et al. (1984) noted that progressions of paleomagnetic poles (which are commonly referred to as apparent polar wander paths; APWPs) have arcing trajectories similar to fracture zones and hotspot tracks. This similar geometry is expected given that they are also tracking plate motion (Fig. 1). Building on the approach of Francheteau and Sclater (1969), Gordon et al. (1984) developed an algorithm to find the best-fit small circles to paleomagnetic poles, which would furnish Euler poles for the plate in question for that time period. This approach for constraining APWPs, called paleomagnetic Euler pole analysis, has the attractive feature of providing a complete description of the plate motion, including paleolongitudinal changes and therefore rates of motion. However, it has the drawback of not providing readily computed uncertainties associated with the paleomagnetic poles and not incorporating age uncertainties. An additional complexity is that while relative motions between tectonic plates can be consistent over extended periods and explained by a single Euler, absolute plate motion relative to the spin axis can be more time variable due to changes associated with one of multiple Euler rotations through a plate circuit or due to a combination of plate tectonic motion and true polar wander. With some notable exceptions (e.g. Bryan & Gordon, 1986; Beck, 1989; Talling & Abdeldayem, 1996; Beck & Housen, 2003; Smirnov & Tarduno, 2010), paleomagnetic Euler pole analysis has not seen wide adoption.

In this contribution, we extend paleomagnetic Euler pole analysis by placing it within a Bayesian statistical framework and demonstrate how to invert for paleomagnetic Euler poles using Markov chain Monte Carlo (MCMC) methods. This framework has the advantage of naturally incorporating uncertainties in paleomagnetic pole positions, as well as widely disparate age uncertainties associated with individual paleomagnetic poles. The resulting stage poles from these inversions are not a single answer, but are instead a distribution of possible answers, furnishing uncertainties as part of the solution process. Proper treatment of uncertainties also allow researchers to avoid overfitting mod-

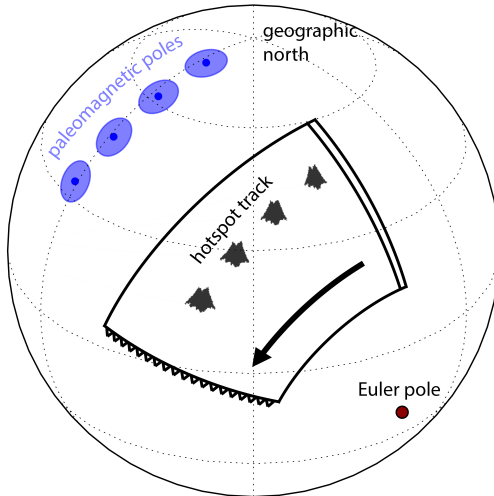


Figure 1. Conceptual model for a paleomagnetic Euler pole. A finite rotation of a plate around an Euler pole (dark red circle) results in arcuate oceanic fracture zones and hotspot tracks (cartoon mountain) which describe small circles on the globe. The same finite rotation produces a circle in the APWP, which is illustrated by blue paleomagnetic poles. By fitting a small/great circle to the APWP, we may recover the Euler pole that produced the rotation which is termed the paleomagnetic Euler pole. Cartoon is adapted from Gordon et al. (1984).

els to noise. For instance, Iaffaldano et al. (2012) employed a similar Bayesian approach to inversions for finite plate rotations. They used seafloor data to reconstruct relative plate motion across Atlantic, Indian and South Pacific ridges incorporating uncertainties into the inversion. In the process, they demonstrated that interpretations of changes in relative plate motions on timescales <1 Myr are the result of overfitting the data and concluded there are fewer kinematic changes and longer stability in plate motions than suggested by some previous treatments.

In the sections below, we first review different approaches that have been applied to synthesize and interpret APWPs. We then describe the formalism of Bayesian inversions and Markov chain Monte Carlo methods that we will apply. We then describe the statistical model which we will be inverting and demonstrate the inversion of several synthetic data sets. Finally, we show case studies where we apply the method to paleomagnetic poles in order to develop estimates of paleomagnetic Euler poles and associated plate motion.

Interpretation of apparent polar wander paths

A sequence of paleomagnetic poles from the same continental block can be synthesized into an APWP, which can then be used to develop plate tectonic reconstructions and models of plate motion with respect to Earth's spin axis through time. Interpretation of these paths becomes difficult in the case of limited, uncertain, or conflicting data, and when the ages of paleomagnetic poles are poorly known. A number of approaches to developing APWPs have been developed, which we briefly review here.

136

Latitudinal drift

137

A paleomagnetic pole provides constraints on the paleolatitude and orientation of a lithospheric block. However, due to the rotational symmetry of Earth's time-averaged geocentric axial dipole magnetic field, paleomagnetic poles do not directly constrain absolute paleolongitude (Butler, 1992). The simplest analysis of an APWP is to compare the paleolatitudes implied by successive poles for a point on a respective block. The difference in paleolatitudes gives a minimum angular distance over which the block has traveled. When this distance is compared to the age difference between the poles, such a comparison establishes a rate of latitudinal motion.

138

139

140

141

142

143

144

It is possible to estimate confidence bounds on the rate of latitudinal drift through bootstrap resampling (e.g. Tarduno et al., 1990) or by taking a Monte Carlo approach. Swanson-Hysell et al. (2014) developed a Monte Carlo sampling method and applied the method to a pair of poles from the Proterozoic Midcontinent Rift of North America to estimate the range of implied latitudinal drift. They also sampled from the uncertainties of radiometric dates associated with the poles, assuming Gaussian distributions, in order to incorporate age uncertainties into the analysis. With samples of pole position and ages, they were able to estimate the 95% confidence estimates on the rate of latitudinal drift.

145

146

147

148

149

150

151

152

153

Whether using point estimates of the latitudinal drift rate or using Monte Carlo estimates, the latitudinal drift interpretation of APWPs remains limited as it represents a minimum estimate of total plate motion. It does not resolve longitudinal drift rate, nor does it naturally extend to APWPs with more than two poles, especially if two coeval poles are not in agreement, as it requires the selection of pole pairs.

154

155

156

157

158

159

Spherical splines

160

161

162

163

When considering APWPs with many poles, it becomes more difficult to perform latitudinal comparisons between pairs of poles. It is not always clear which pairs of poles to compare in cases where there are many overlapping paleomagnetic poles that have variable uncertainties associated with their positions and ages.

164

165

166

167

168

169

170

171

172

173

174

One approach to synthesize such data is to fit a spline through the set of paleomagnetic poles, constraining the path to lie on the surface of a sphere. This approach was pioneered by Torsvik et al. (1992) using the spherical spline algorithm developed by Jupp and Kent (1987). This approach has the advantage of allowing the paleomagnetic poles to be weighted by their spatial uncertainties. The uncertainty assigned to a paleomagnetic pole can be the 95% confidence interval on the pole position, but it can also be augmented by various quality screening factors, such as the quality ("Q") factor of Van der Voo (1990) (Torsvik et al., 1992). Even with the weighting of the paleomagnetic poles by uncertainty, there can be unrealistic loops in the APWP generated by the spline fit. To combat this behavior, the spline can also be computed under tension which penalizes curvature and produces a smoother path (Torsvik et al., 1996).

175

176

177

178

179

180

181

182

183

184

The spherical spline approach to interpreting APWPs has attractive features. It produces a smooth path through the data that can incorporate spatial uncertainties, and may be efficiently computed. However, it does have some drawbacks. It is not easy to determine the appropriate uncertainty weighting and spline tension parameters for the fit, and what effect those choices have on the result. Furthermore, the resulting fit does not have an uncertainty with a physically interpretable meaning (Torsvik et al., 1996). It also does not have a simple way of incorporating age uncertainties of the paleomagnetic poles. Finally, by their nature, splines do not readily represent the sharp hairpin cusps that characterize abrupt shifts in motion that plates sometimes undergo (Irving & Park, 1972; Gordon et al., 1984; Torsvik et al., 2012).

185 **Running means**

186 An alternative method for developing APWPs is to perform a running Fisher mean
 187 on the poles with a moving window through time (Irving, 1977; Van der Voo & Torsvik,
 188 2001; Torsvik et al., 2008). In such an analysis, paleomagnetic poles in a compilation are
 189 averaged with a defined window duration (typically 10-30 Myr) that controls the amount
 190 of smoothing. Like spherical splines, the running mean approach has the ability to ef-
 191 fectively damp the effect of outlier poles that could lead to spurious motion in the APWP
 192 if there are sufficient data. Torsvik et al. (2008) also investigated the effects of combin-
 193 ing running means with spherical splines, by first computing a set of mean poles and then
 194 fitting a spline through those means. The simplicity of using the running mean approach
 195 to develop an APWP, as well as its ability to suppress potentially spurious poles, has
 196 led to it being widely adopted.

197 While it is a straightforward approach with advantages for synthesizing paleomag-
 198 netic poles, the running mean approach shares many of the drawbacks of the spline ap-
 199 proach. As with the spherical spline method, age uncertainties on the poles are not in-
 200 corporated, nor are the uncertainties in pole positions as typically implemented. It is not
 201 obvious how to best choose the window duration, and different window durations are likely
 202 appropriate for different data sets. It is also unclear how to interpret the resulting un-
 203 certainties in the path that are reported as a Fisher A_{95} ellipse of the mean of the poles
 204 as the poles need not be coming from a Fisher distribution particularly if there is on-
 205 going plate motion. A recent study discussed the advantage that could be gained by cal-
 206 culating APWPs from site level data (virtual geomagnetic poles) rather than from study
 207 level mean paleomagnetic poles (Vaes et al., 2022). This work highlighted how such an
 208 approach could ameliorate the disadvantage of typical running mean approaches of giv-
 209 ing equal weight to study level poles which themselves comprise varying numbers of site
 210 level virtual geomagnetic poles.

211 **Paleomagnetic Euler poles**

212 The idea of fitting small circles to paleomagnetic data to gain insight into plate mo-
 213 tions was first described by Francheteau and Sclater (1969). The center of such a cir-
 214 cle on a sphere is the pole of rotation which was termed a paleomagnetic Euler pole by
 215 Gordon et al. (1984) who developed a method to invert for the position of such poles.
 216 The approach builds on the recognition that plate motions can often be approximated
 217 by finite rotations around Euler poles which can potentially be steady for millions or tens
 218 of millions of years. As a result, an arcuate APWP of a plate can be described by Eu-
 219 ler rotations, which produce small circle paths on Earth's surface if the Euler pole re-
 220 mains in a relative constant position (Fig. 1). Since the analysis solves for the Euler pole
 221 that produces a given small circle, this approach allows for an estimate of the full mo-
 222 tion of a given plate, including the total plate speed (instead of just the latitudinal com-
 223 ponent of the speed). Effectively, the analysis utilizes both the change in plate orienta-
 224 tion and latitude information embedded within paleomagnetic poles to estimate both lat-
 225 itudinal and longitudinal motion as succinctly specified by Euler pole parameters.

226 However, paleomagnetic Euler pole analysis has many of the same deficiencies that
 227 spline fits and running means have—it is not easy to compute uncertainties, especially
 228 in the presence of unknown ages of poles. Furthermore, one has the additional challenge
 229 and related uncertainty of deciding how many paleomagnetic Euler poles to include for
 230 a given sequence of paleomagnetic poles. In most treatments, this number of stage poles
 231 is subject to researcher choice (however, see theoretical progress in this regard by Gallo
 232 et al. (2022)). In this contribution, we develop a Bayesian statistical approach to paleo-
 233 omagnetic Euler pole analysis which attempts to address some of these deficiencies.

234 **Bayesian inversion**

235 **A general description of inverse problems**

The central question motivating inverse problems is “How probable is a particular model, given my observations?”. We represent observations by the data vector \mathbf{d} , and a model by the vector of model parameters \mathbf{m} , so the above question can be expressed as the function $P(\mathbf{m}|\mathbf{d})$ (the probability of the model given the data). Traditional frequentist approaches to an inverse problem often proceed by maximizing the likelihood function, defined by the probability of the data given a particular model (e.g. Aster et al., 2005):

$$\mathcal{L}(\mathbf{m}|\mathbf{d}) \equiv P(\mathbf{d}|\mathbf{m}). \quad (1)$$

The likelihood function replaces something that is difficult to compute (namely, $P(\mathbf{m}|\mathbf{d})$) with something that is less difficult to compute. To compute $\mathcal{L}(\mathbf{m}|\mathbf{d})$ we need to have two things: a statistical model for uncertainties in the observations \mathbf{d} and a forward model that allows us to compute predictions. We denote the forward model by \mathbf{g} :

$$\mathbf{d}^p = \mathbf{g}(\mathbf{m}), \quad (2)$$

where the superscript “ p ” denotes a predicted value. If each of the observed data d_i are described by Gaussian random variables with standard deviations σ_i , the likelihood function is given by the product of the individual likelihoods of the observations:

$$\mathcal{L}(\mathbf{d}|\mathbf{m}) = \prod_i \exp\left(-\frac{(d_i - d_i^p)^2}{2\sigma_i^2}\right). \quad (3)$$

The likelihood function \mathcal{L} is maximized by searching over the model parameter space. If the uncertainties in the observations are Gaussian, then maximizing the likelihood function is equivalent to the least squares solution (Aster et al., 2005).

A standard maximum likelihood fit will frequently overfit the observations, resulting in unrealistic solutions. In the context of APWPs, these overfit solutions may pass through every paleomagnetic pole, including less reliable ones, resulting in loopy or jerky paths. In order to address such overfitting, some form of regularization is usually included in the solution of the inverse problem, such as penalizing the magnitude or curvature of the solution. Both the running-mean and the spline under tension approaches to AP-WPs are forms of regularization on the problem.

246 **Bayesian approach**

The Bayesian approach to inverse problems takes a different strategy from the frequentist one. Rather than finding a model with parameters that maximize the likelihood, it treats the underlying model as a set of random variables with individual probability distributions. The probability distribution of the model given the data ($P(\mathbf{m}|\mathbf{d})$) is then found by an application of Bayes theorem (cf. Sivia & Skilling, 2006):

$$P(\mathbf{m}|\mathbf{d}) = \frac{P(\mathbf{d}|\mathbf{m}) P(\mathbf{m})}{P(\mathbf{d})}. \quad (4)$$

It is often unnecessary to calculate the denominator of Equation 4, which is a normalization constant, leaving us with

$$P(\mathbf{m}|\mathbf{d}) \propto P(\mathbf{d}|\mathbf{m}) P(\mathbf{m}). \quad (5)$$

The quantity $P(\mathbf{m}|\mathbf{d})$ is known as the posterior probability, and it represents our desired knowledge about the distributions of the parameters \mathbf{m} . The first factor on the right-hand-side of Equation 5 is identical to the likelihood function described above, and the second factor is known as the prior probability of the model. In the case for Euler pole

and/or true polar wander inversions, our model parameters are Euler pole positions (longitudes, latitudes) and rotation rate as well as changepoints (when multiple rotations are inverted for).

In this case, the prior probability distributions reflect the state of our knowledge and beliefs of the values of the Euler rotation axes and rotation rates prior to the consideration of data. It allows us to incorporate theoretically or empirically derived constraints that are not otherwise included in the forward model. In contrast with the classical statistical approach of regularization, the Bayesian inverse problem can (in effect) regularize the problem by making choices of probability distributions that have less probability density in parameter space with less realistic values (e.g. Minson et al., 2013; Sambridge et al., 2013).

Markov chain Monte Carlo methods

For complex models, it is usually impossible to calculate the posterior probability distribution in Equation 4 directly (Davidson-Pilon, 2015). It is much more tractable to generate a Markov chain which, upon convergence, generates samples from the desired posterior distribution (Gelman et al., 2013). This approach defines a class of methods known as Markov chain Monte Carlo (MCMC) methods.

In comparison with drawing Monte Carlo resamples from random variables independently, Markov chain Monte Carlo resampling generates a sequence of samples where the current value for each variable is dependent on its prior value. This approach allows for more efficient sampling of probability distributions with sampling that converges towards higher posterior probabilities. For an introduction to MCMC methods, the interested reader could refer to Gelman and Rubin (1996), Sambridge et al. (2013), and Davidson-Pilon (2015). A number of high-quality open source software packages for implementing MCMC models exist, including WinBUGS (Lunn et al., 2000), PyMC (Salvatier et al., 2016), and Stan (Carpenter et al., 2017). We make extensive use of PyMC in this work.

Distributions on a sphere

In order to proceed with a Bayesian description of the problem, every parameter in the model needs to be described by some statistical distribution that determines the probability that the parameter takes a specific value. Parameters like pole ages can be described by 1D probability distributions (such as uniform or normal distributions), whereas Euler pole locations are described by 2D distributions of directional data on the surface of a sphere. We review several of these distributions here. For a comprehensive discussion of spherical probability distributions, see Fisher et al. (1987). Plots of the following distributions (uniform, Fisher, and Watson), as well as samples drawn from them, are shown in Figure 2.

Uniform distribution

The simplest probability distribution on a sphere is the spherical uniform distribution. It has a probability density given by

$$\rho_U(\phi, \psi) = \frac{1}{4\pi} \cos \psi \text{ or } \rho_U(\hat{\mathbf{x}}) = \frac{1}{4\pi} \quad (6)$$

where ρ_U is the probability density, ϕ is the longitude, and ψ is the latitude (we refer to the Cartesian unit vector $\hat{\mathbf{x}}$ as a concise representation of ϕ and ψ). Non-uniform distributions on a sphere reduce to the uniform distribution in some limit (i.e. the Fisher distribution as the precision parameter goes to zero). We use the uniform distribution when we want to specify an uninformative prior distribution for directional parameters.

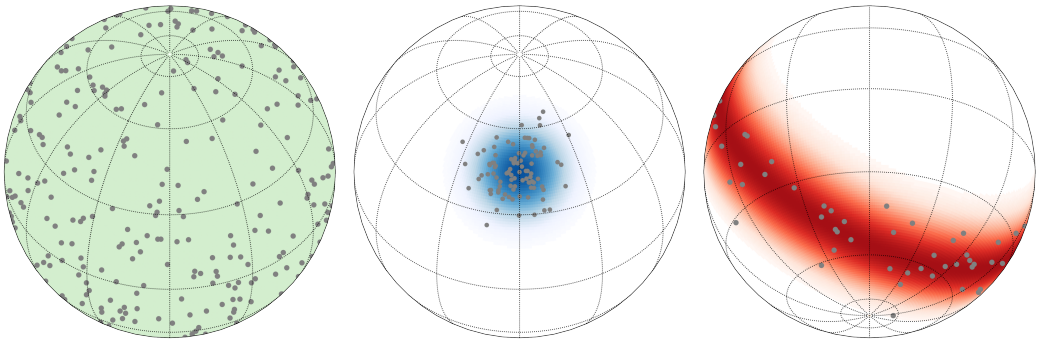


Figure 2. Probability densities for distributions of directional data, as well as samples drawn from them. All distributions are plotted using an orthographic projection. (left panel) Uniform distribution. (middle panel) Fisher distribution. The center of the distribution is at 45°N, 30°E, with concentration parameter of $\kappa_F = 50$. (right panel) Watson girdle distribution. The pole of symmetry is at 30°N, 30°E, with a concentration parameter of $\kappa_W = -25$.

294

Fisher distribution

The Fisher distribution (also called the von Mises-Fisher distribution) is the analogue of a 2D normal distribution on a sphere (Fig. 2). The probability density ρ_F at a point $\hat{\mathbf{x}}$ is given by

$$\begin{aligned}\rho_F(\phi, \psi; \kappa_F, \hat{\mu}) &= \frac{1}{C_F} \exp(\kappa_F \hat{\mathbf{x}}^T \hat{\mu}) \\ &= \frac{1}{C_F} \exp(\kappa_F \cos \theta),\end{aligned}\quad (7)$$

where κ_F is the concentration of the distribution, $\hat{\mu}$ the unit vector for the mean direction of the distribution, and C_F is a normalization coefficient. It can be alternatively parameterized using θ , which is the angle between $\hat{\mathbf{x}}$ and $\hat{\mu}$. The normalization factor is given by

$$C_F = \frac{\kappa_F}{4\pi \sinh \kappa_F}. \quad (8)$$

295
296

When κ_F goes to zero, the Fisher distribution is equivalent to the spherical uniform distribution.

297
298
299

The uncertainty ellipses for paleomagnetic poles are typically calculated assuming a Fisher distribution of the underlying data, and we will use this distribution to calculate the likelihood function for pole positions in the model.

300

Watson girdle distribution

Whereas the Fisher distribution concentrates probability density around a pole on the surface of the sphere, the Watson girdle probability distribution is concentrated in a belt orthogonal to the pole (Fig. 2). It is useful for characterizing planar data, and is given by

$$\begin{aligned}\rho_W(\phi, \psi; \kappa_W, \hat{\mu}) &= \frac{1}{C_W} \exp(\kappa_W (\hat{\mathbf{x}}^T \hat{\mu})^2) \\ &= \frac{1}{C_W} \exp(\kappa_W \cos^2 \theta),\end{aligned}\quad (9)$$

301
302
303
304

where κ_W is the concentration of the girdle, C_W is a normalization coefficient, and the other parameters are identical to those in the Fisher distribution. The Watson distribution is girdle-shaped only when κ_W is a negative number, which is the only case we consider here.

The normalization factor is given by

$$C_W = \left[{}_1F_1\left(\frac{1}{2}, \frac{3}{2}, \kappa_W\right) \right]^{-1}, \quad (10)$$

where ${}_1F_1()$ is Kummer's confluent hypergeometric function, which is available in most software libraries of special mathematical functions. As with the Fisher distribution, when κ_W goes to zero, the Watson distribution is equivalent to the spherical uniform distribution.

309 A model for paleomagnetic Euler pole inversion

310 Forward model

311 A forward model describes how we generate predicted observations given a set of
 312 model parameters (Equation 2). The forward model for paleomagnetic Euler pole analysis
 313 in this study is essentially unchanged from that of Gordon et al. (1984). We will con-
 314 sider three overall scenarios of plate motions (and hence paleomagnetic pole motions).
 315 The first is that plate motion is the result of plate tectonic motion about an Euler pole
 316 or a series of Euler poles. Each Euler pole has three parameters: a latitude, a longitude,
 317 and a rotation rate. In a model with multiple Euler poles, we also must specify the ages
 318 where one Euler pole switches to the next as an additional unknown variable. In the con-
 319 text of parameter inversion, these ages are often known as “changepoints.” For plate tec-
 320 tonic motions, the motion can be along any plane intersecting the sphere such that they
 321 are small circles. The second scenario we will consider is one wherein the sole cause of
 322 the motion of paleomagnetic poles is true polar wander in which case motion is restricted
 323 to be along a great circle path coaxial to the axis of minimum inertia (Creveling et al.,
 324 2012). In such a model, three parameters exist: a latitude and a longitude of the true
 325 polar wander rotation axis and a rotation rate. A third scenario is that plate tectonic
 326 and true polar wander rotations are occurring concurrently leading to an observed pa-
 327 leomagnetic pole path.

328 We also need to initiate a model with a starting position on the globe, which, in
 329 practice, can be sampled from the Fisher distribution of the oldest paleomagnetic pole
 330 in the data set. The starting point contributes two parameters (a latitude and a longi-
 331 tude).

Therefore, a model with n_e Euler rotations will have $3n_e$ parameters for the poles,
 $(n_e - 1)$ parameters for the changepoints, and 2 parameters for the starting location.
 The number parameters for which we are inverting is then given by

$$\begin{aligned} N &= 3n_e + (n_e - 1) + 2 \\ &= 4n_e + 1. \end{aligned} \quad (11)$$

Two more parameters will be included in a model where true polar wander is considered to happen on top of n_e Euler rotations. In this case, the axis of true polar wander is constrained to be on a great circle that is orthogonal to the vector representing the starting pole position. Therefore, a total of $4n_e + 3$ parameters are inverted for.

With the axes and rates for such spherical rotations defined, one can calculate the linear velocity \mathbf{v} of a point \mathbf{p} on the surface of the globe associated with angular velocity ω_i by

$$\mathbf{v} = \omega_i \times \mathbf{p}. \quad (12)$$

Finite rotations can be performed by constructing Euler angle rotation matrices
 (cf. Goldstein, 1965). We generate synthetic paleomagnetic pole positions from the for-
 ward model by stringing together finite rotations through the stage poles until the age

339 of the observed paleomagnetic pole is reached. These positions can then be compared
 340 to the observed paleomagnetic poles in a given dataset.

341 Choice of prior distributions

342 Bayesian analysis requires us to specify prior probability distributions for each of
 343 the model parameters in the inverse problem. These distributions reflect our state of knowl-
 344 edge about the values of the parameters before we begin, and allow us the option of in-
 345 corporating information otherwise not captured by the model. To avoid biasing the re-
 346 sults of the model towards a specific posterior distribution, we usually try to choose prior
 347 distributions that are as uninformative as possible. Depending upon the context, and
 348 the type of parameter, that choice may vary. The central parameters in the paleomag-
 349 netic Euler pole problem are the Euler pole positions, the Euler pole magnitudes, the
 350 changepoints, the starting point, and the paleomagnetic pole ages, which we treat in turn.
 351 We use the notation $x \sim y$ to indicate that the parameter x is drawn from distribution
 352 y .

Euler rotation vectors: The first parameter we consider is the position of the Euler poles, which should be drawn from a spherical probability distribution. The least informative prior distribution for an Euler pole position is the uniform spherical distribution:

$$\hat{\omega}_i \sim \rho_U. \quad (13)$$

353 essentially allowing the Euler pole to be anywhere on the globe with equal probability.

354 An alternative choice is to inform our prior distribution for Euler pole positions based
 355 on observation of modern plate motions. It has long been observed that, to first order,
 356 plate motions are well explained by slab-pull torques acting along subduction zones, and
 357 to a lesser extent, ridge push and mantle traction effects (Forsyth & Uyeda, 1975; Gor-
 358 don et al., 1978; Richardson, 1992).

359 We can ask the question of whether the Euler pole for a given plate is more likely
 360 to be on top of the plate (corresponding to a spinning motion for that plate) or away
 361 from that plate (corresponding to motion across the surface of Earth). Given that tec-
 362 tonic plates can broadly be considered to be the surface expression of mantle convection,
 363 we can hypothesize that the second possibility is more likely because a spinning plate
 364 has no divergence (i.e., spreading centers and subduction zones, (Forte & Peltier, 1987;
 365 Gable et al., 1991). Without divergence, the plate motion does not contribute to large-
 366 scale convection.

367 To evaluate this hypothesis, we generated position samples on the surface of Earth
 368 and computed the angular distance between that point and the Euler pole for the plate
 369 in which that point resides. We used the NNR-MORVEL56 model for current plate mo-
 370 tions (Argus et al., 2011) and restricted our analysis to the fourteen largest plates. We
 371 then fit those angular distance samples to a Watson girdle distribution (Equation 9), in-
 372 verting for the concentration parameter κ_W . If an Euler pole position has no preference
 373 for being a particular angular distance from a point on a plate, then κ_W should be close
 374 to zero, corresponding to a uniform distribution. We find that the distribution is best
 375 fit with $\kappa_W \approx -0.7$, which corresponds to the Euler pole probability density being roughly
 376 twice as large 90° away from a given point than on top of the point (Fig. 3).

Euler rotation magnitudes: The magnitude of each Euler pole rotation is a pos-
 377 itive number, specifying the rotation rate about the Euler pole (negative magnitudes can
 378 be accommodated by flipping an Euler pole to the antipode). There are several possi-
 379 bilities for the prior distribution for the rates. In order to not bias the inversion towards
 380 a particular rate, we can choose a uniform prior distribution with large support:

$$|\omega_i| \sim U(\cdot, \cdot), \quad (14)$$

377 where $U(\cdot, \cdot)$ is a uniform distribution between two values, and is specified in degrees per
 378 million years. Typical rotation rates for present day plate motions are under $1^\circ/\text{Myr}$ (Argus
 379 et al., 2011), which corresponds to plate speeds of about 11 cm/yr for a rotation about
 380 an Euler pole that is 90° from a plate.

Another option is to choose a weakly informative prior distribution for the Euler pole magnitudes informed by recent plate motions (similar our approach of the Watson girdle prior distribution for Euler pole position). Zahirovic et al. (2015) found, based on analysis of Cenozoic and Mesozoic plate reconstructions, that plate speeds much higher than 15 cm/yr were unlikely to be sustained. A reasonable choice of distribution for strictly positive numbers is the exponential distribution, given by

$$\rho_E(|\omega_i|) = \lambda \exp(-\lambda|\omega_i|), \quad (15)$$

381 which has higher probability density at lower values, and falls off exponentially toward
 382 higher values. We sampled the current plate rates on Earth's surface according to NNR-
 383 MORVEL56 and fit those to an exponential distribution. The best fitting scale parameter
 384 λ for current plate rates is ~ 2.5 (Fig. 3). Making this choice of prior distribution
 385 for Euler pole rotation rates can be seen as a form of regularization on plate speeds. A
 386 smaller for λ (such as $\lambda = 1$ as is shown in Fig. 3) could reflect similar knowledge about
 387 the distribution of plate speeds with a less restrictive regularization.

Changepoints: Changepoints occur sequentially between the oldest (at age a_{\max}) and youngest (at age a_{\min}) paleomagnetic poles. We choose a uniform distribution as a prior for these changepoints:

$$c_i \sim U(a_{\min}, a_{\max}), \quad (16)$$

388 where c_i is the i'th changepoint.

Starting position: Finally, the starting position $\hat{\mathbf{x}}_{\text{start}}$ for the set of Euler pole rotations needs a prior distribution. We could choose another uniform distribution, but a more reasonable choice is to start near the oldest paleomagnetic pole in the dataset. We therefore choose the Fisher distribution of the oldest paleomagnetic pole as a reasonable prior distribution for a start point:

$$\hat{\mathbf{x}}_{\text{start}} \sim \rho_F(\kappa_{F0}, \hat{\mu}_0), \quad (17)$$

389 where κ_{F0} and $\hat{\mu}_0$ are the concentration parameter and mean direction of the oldest pa-
 390 leomagnetic pole in the dataset.

391 **Pole ages:** One of the major advantages of Bayesian analysis is the ability to nat-
 392 urally incorporate uncertainties in as many parameters as needed. Previous approaches
 393 to modeling APWPs have the drawback that they do not easily account for uncertain-
 394 ties in the age of paleomagnetic poles. In our approach, we can include age uncertainty
 395 by including the age of the poles and associated uncertainty as parameters in our model.

There are many different ways to constrain the ages of the geologic units from which we obtain paleomagnetic poles, including radiometric dating, biostratigraphy, magnetostratigraphy, and cross-cutting relationships. Here we concentrate on poles that are either interpreted to be the age of a single radiometric date or are interpreted to be bracketed stratigraphically between two dates (derived radiometrically or by using other age control such as biostratigraphy). If a geologic unit has been radiometrically dated, we can model the age of the j'th paleomagnetic pole a_j as a normal distribution with mean μ_j and standard deviation σ_j :

$$a_j \sim N(\mu_j, \sigma_j), \quad (18)$$

396 where $N(., .)$ denotes a normal distribution.

Frequently, however, the geologic unit from which we obtain a paleomagnetic pole is not well dated, but its age can be constrained to lie between those of well-dated units

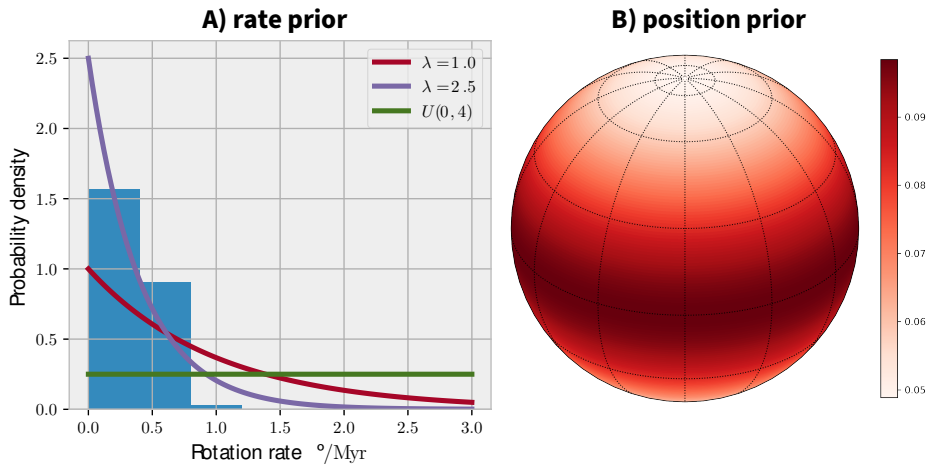


Figure 3. Informative prior distributions for Euler poles. (a) Prior probabilities for rotation rates. The histogram is the angular rotation rate from one thousand samples from the surface of Earth, using the NNR-MORVEL56 model. A fit to this sample set with an exponential distribution yields a scale parameter of $\lambda \approx 2.5$. We also show the distribution for $\lambda = 1.0$, which imposes less regularization on the rate as a less restrictive prior distribution, and a uniform $U(0, 4)$ distribution between 0 and $4^{\circ}/\text{Myr}$, which specifies no preference for slower speeds if set as the prior probability. (b) Prior probability density for the position of the Euler poles, with the north pole as the site latitude and longitude. We again sampled one thousand points on Earth's surface, calculating the angular distance between that point and the Euler pole for its plate. If we model the probability distribution as being drawn from a Watson distribution, these angular distances correspond to colatitudes, where the pole is the sampled point. Fitting the resulting angular distribution to a Watson girdle distribution finds $\kappa_W \approx -0.7$. Since the Watson distribution is rotationally symmetric, longitudes do not contribute to the fit. For $\kappa_W \approx -0.7$ the probability density is roughly twice as large at the equator (90° from a plate) as at the pole (on top of the plate).

stratigraphically above and below it, dates obtained by cross-cutting relationships, or a number of dated units within a broader province. In these cases, a uniform distribution between those ages is a reasonable choice for the prior distribution:

$$a_j \sim U(a_{\text{young}}, a_{\text{old}}), \quad (19)$$

where a_{young} and a_{old} are the ages of the lower and upper age constraints, respectively.

True polar wander: Another advantage of this method is the ability to also incorporate a component of true polar wander rotation on top of Euler pole rotations. Because true polar wander represents the rotation of the entire solid Earth with respect to the spin axis, an APWP that is solely consisted of true polar wander should follow a great circle trajectory and the associated rotation axis should be orthogonal to the great circle. In a case where both small circle rotations and true polar wander are recorded by an APWP, the true polar wander rotation axis is constrained to be 90° away from the start position of the path and the rotation rate can be defined in a similar fashion as that of the Euler pole magnitudes.

To summarize our choices for prior distributions:

- Euler pole positions: spherical uniform distribution, or a Watson girdle distribution with $\kappa_W \approx -0.7$.
- Euler pole magnitudes: Uniform distribution, or an exponential distribution with $\lambda \approx 2.5$ or smaller.
- Changepoints: uniform distribution between a_{\min} and a_{\max} .
- Starting position: Fisher distribution usually defined by the Fisher statistics of the oldest paleomagnetic pole position in an APWP.
- Paleomagnetic pole ages: normal or uniform distribution, depending on the type of age control for the geologic unit from which the pole was obtained.

Likelihood

In addition to the choice of prior distributions, we need a statistical description of the observations. This description will allow us to calculate the likelihood function, which, when combined with the prior distributions, allows us to evaluate Bayes' theorem (Equation 5).

In the case of APWPs, our observations are paleomagnetic poles. The most common statistical distribution for describing paleomagnetic poles is the Fisher distribution (although other distributions are sometimes used, such as the Kent or Bingham distributions, c.f. Tauxe (2010)). Given the set of model parameters \mathbf{m} and the forward model $\mathbf{g}(\mathbf{m})$, described above, we can calculate the predicted paleomagnetic pole unit vectors $\hat{\mathbf{x}}_i^p$. For a set of n paleomagnetic poles, the likelihood is then given by the product of the probabilities of each observation of paleomagnetic pole position:

$$P(\mathbf{d}|\mathbf{m}) = \prod_{i=1}^n \frac{1}{C_{F,i}} \exp \left(\kappa_{F,i} \hat{\mathbf{x}}_i^{pT} \hat{\mu}_i \right). \quad (20)$$

Example inversions

Before proceeding with inversions for paleomagnetic Euler poles using real paleomagnetic data, it is useful to consider a few examples of inversions for idealized synthetic datasets. We have specified the forward model described above using the package PyMC (Salvatier et al., 2016) which enables us to perform the inversion. Within PyMC, we are able to specify custom probability distributions enabling the directional data distributions illustrated in Figure 2 to be implemented. The Markov chain Monte Carlo (MCMC)

429 analysis uses the Metropolis–Hastings algorithm for sampling as it can be applied to cus-
 430 tom probability distributions in contrast with other sampling algorithms within PyMC.
 431 Our code for the inversions has an open-source GPL license and is available on Github
 432 (https://github.com/Swanson-Hysell-Group/Bayesian_PEP_inversion) and archived
 433 on Zenodo (*we will archive the Github repository on Zenodo at the time of proofs fol-*
 434 *lowing any revisions which provides long-term assurance of archival and will add the link*
 435 *here*).

436 One Euler rotation

437 We begin by trying to recover the Euler pole for a single rotation. We generate an
 438 idealized synthetic APWP of four poles by starting from a pole at 19° N, 024° E, and
 439 rotating around an Euler pole at 00° N, 000° E for 100 Myr at a rate of $1^\circ/\text{Myr}$. We pro-
 440 duce paleomagnetic poles at 100 Ma, 75 Ma, 50 Ma, and 25 Ma, and prescribe A_{95} of
 441 4° to each pole (where A_{95} indicates the 95% angular confidence for the pole position).

442 To demonstrate the ability to recover the Euler rotation axes and rotation rate us-
 443 ing the inversion method, we introduce minimal prior knowledge on these parameters,
 444 but assume the ages of the paleomagnetic poles are well constrained. Therefore, we use
 445 a Watson girdle distribution with $\kappa_W = -0.1$ (more weakly informative than -0.7 of Fig.
 446 3 and approaching a uniform distribution as illustrated in Fig. S2) as the prior distri-
 447 bution for the Euler rotation axis, and a uniform distribution of $U(0, 4)$ as the prior dis-
 448 tribution for the Euler rotation rate (in $^\circ/\text{Myr}$).

449 The results of the inversion are shown in Figure 4. The Bayesian approach success-
 450 fully recovers a posterior probability distribution for the position of the Euler pole, as
 451 well as a rate that is centered near the true value of $1^\circ/\text{Myr}$ (Fig. 4B). The posterior dis-
 452 tribution for the rate has a highest posterior density credible interval at 95% (which we
 453 abbreviate from here as a 95% credible interval) between $0.7^\circ/\text{Myr}$ and $1.2^\circ/\text{Myr}$, re-
 454 flecting the resolving power of the inversion for data with the given uncertainties. An
 455 example of this same inversion with simulated noise on the age and position of paleo-
 456 magnetic poles is developed in PEP_synthetic.ipynb within the archived code repository
 457 and shown in Figure S1. It is also successful in recovering the true values within the cred-
 458 ible intervals of the posterior distributions.

459 Two Euler rotations

460 We next consider an inversion for an APWP with two stage poles. Unlike the pre-
 461 vious example where we inverted for a single Euler pole, this inversion also requires a
 462 changepoint. We generate nine idealized paleomagnetic poles with A_{95} of 4° for each from
 463 a starting point at 5°S , 030°E . The first rotation is around an Euler pole at 10°S , 000°E ,
 464 and rotates at $1.5^\circ/\text{Myr}$ for 60 Myr. The second rotation is around an Euler pole at 10°N ,
 465 300°E and rotates at a rate of $0.75^\circ/\text{Myr}$ for the same amount of time. The synthetic
 466 poles associated with this two stage model are shown in Figure 4.

467 During the inversion, the prior knowledge for the Euler rotation axes and rates and
 468 the age of the paleomagnetic poles are set in the same way as in the one Euler rotation
 469 section above. The prior distribution for the changepoint is set as a uniform distribu-
 470 tion with the minimum and maximum ages being the age of the youngest and oldest pa-
 471 leomagnetic poles.

472 The inversion successfully recovers the Euler pole rotation rates with posterior dis-
 473 tributions centered near the true values. The inversion also successfully recovers the change-
 474 point of 60 Ma between the first and second Euler pole with a 95% credible interval for
 475 the changepoint of 65 to 55 Ma. The inverted Euler pole positions for the first stage pole
 476 (blue distributions in Fig. 4C) are centered near the true location (blue star in Fig. 4C)
 477 and the inverted second Euler pole positions (red distributions in Fig. 4C) encompass

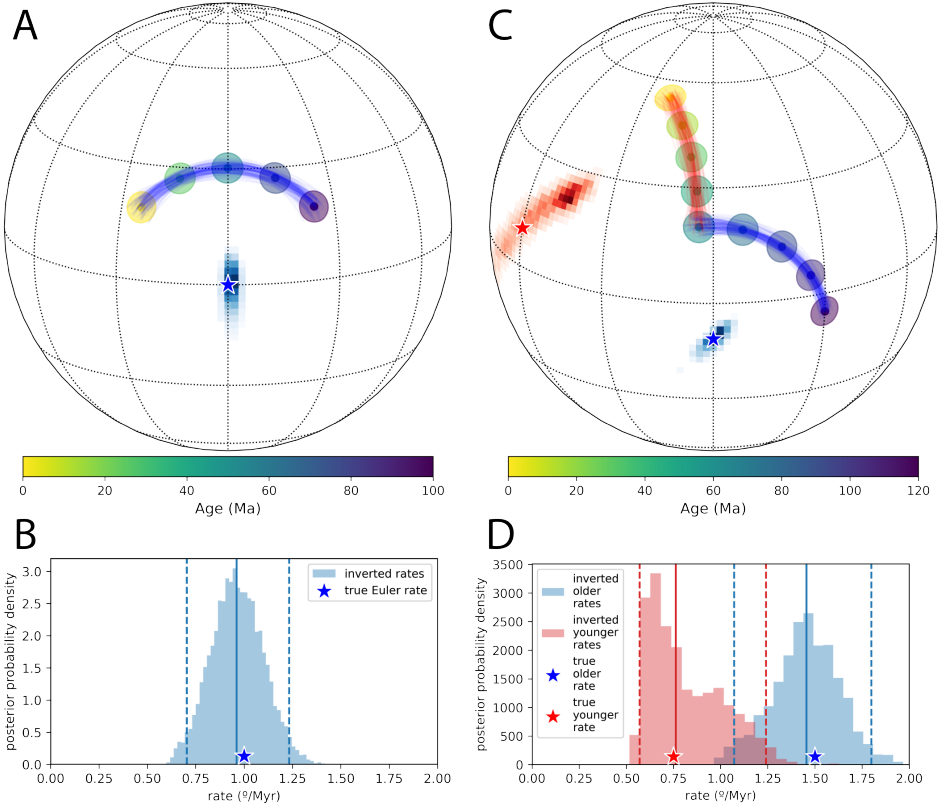


Figure 4. Inversion for Euler poles from synthetic data. (A) Five paleomagnetic poles are generated during a net 100° rotation about an Euler pole at 0°N , 0°E over 100 Myr, for a rotation rate of $1^\circ/\text{Myr}$. The blue distribution is the probability density of Euler pole positions recovered by MCMC inversion, and the blue arcs are 100 of the resulting synthetic APWPs (sampled from 50,000). The color bar scale associated with the probability density is shown in a supporting information version of this figure (Fig. S3). Such supporting information figures are provided for every Euler pole position plot in the paper (Figs S3 to S6). (B) Posterior probability density for the rotation rate of the Euler pole recovered by the inversion. The solid line shows the median of the distribution ($0.96^\circ/\text{Myr}$), and the dashed lines show the 95% credible interval ($0.70^\circ - 1.23^\circ/\text{Myr}$). (C) Paleomagnetic poles generated using two distinct Euler poles. The first Euler pole is located at 10°S , 0°E (blue star), and rotates at $1.5^\circ/\text{Myr}$ for 60 Myr. The second Euler pole is located at 10°N , 300°E (red star), and rotates at $0.75^\circ/\text{Myr}$ for 60 Myr. The blue and red distributions show the posterior estimate location of the first and second Euler poles (respectively) recovered by the MCMC inversion. The blue and red arcs are 100 of the synthetic APWPs. (D) Posterior probability density for the rotation rates of the Euler poles recovered by the inversion. The solid lines show the median values of the distributions ($\sim 1.45^\circ/\text{Myr}$ and $0.76^\circ/\text{Myr}$ for Euler rotation 1 and 2), and the dashed lines show the 95% credible intervals.

478 the true location as well (red star in Fig. 4C). There is a larger spread in credible Eu-
 479 ler pole positions for the second Euler pole particularly in the direction perpendicular
 480 to the APWP. The greater uncertainty on the location of the second Euler pole results
 481 from the motion along the APWP being smaller relative to the uncertainty on the pa-
 482 leomagnetic pole positions. As a result, the inverted paths have more variable curvature.

483 Overall, this example demonstrates that the inversion framework can resolve AP-
 484 WPs with more than one stage pole and provides posterior probability distributions on
 485 the Euler rotation changepoint in addition to the multiple Euler poles positions and rates
 486 (Fig. 4C,D).

487 Incorporating age uncertainty

488 A benefit of the Bayesian approach to inverse problems is its generality. As long
 489 as some effect can be described statistically and incorporated into our forward model,
 490 we can include it in the inverse problem. As a result, we are able to include uncertain-
 491 ties on the ages of paleomagnetic poles. Assigning a fixed single age to paleomagnetic
 492 poles can bias an analysis when the age of a pole is not precisely known. The inversion
 493 framework enables the varying certainty on pole ages to be incorporated into the anal-
 494 ysis. To demonstrate this capability, we use a similar test case as in the one Euler pole
 495 inversion with the ages of synthetic poles being adjusted to span from 140 Ma to 40 Ma
 496 (poles of 140, 115, 90, 65, and 40 Ma) (Fig. 5A), but assign prior distributions for the
 497 ages of the poles. For the first and last poles, we assume they are radiometrically dated
 498 with standard deviations of 5 Myr. However, we assume that the middle three poles have
 499 no age control, except that their ages are constrained to be between the first and last
 500 poles. We thus assign Gaussian prior distributions to the first and last poles and uni-
 501 form prior distributions to the middle three (Fig. 5B). Despite this uninformative prior
 502 distribution on the age of the middle three poles, the inversion successfully places the
 503 estimated distributions of ages of the middle three poles to be centered at *ca.* 115 Ma,
 504 *ca.* 90 Ma, and *ca.* 65 Ma as can be seen in their posterior age distributions (Fig. 5D).

505 For real data, adding uncertainties to the ages of the poles enables us to properly
 506 represent our knowledge of the constraints on the APWP. These uncertainties enable data
 507 to constrain the location of the path without providing an overly tight constraint on the
 508 timing when the true age is uncertain. The resulting posterior distributions provide pre-
 509 dicted ages for the poles associated with Euler pole inversions (Fig. 5D).

510 Reporting the apparent polar wander path

A difficulty with the Bayesian approach is that the credible interval of Euler pole
 posterior positions are not easy to report as they do not neatly correspond to a para-
 metric statistical distribution. We visualize the solutions with spatial histograms for the
 Euler pole positions and by showing example inverted paths. A typical product that one
 is seeking with such an inversion is an apparent polar wander path reported as interpreted
 pole position at given intervals. An approach that can be taken is to calculate a num-
 ber of predicted pole positions at a given time implied by inverted Euler pole models and
 then to calculate the Fisher mean of these inverted pole positions as was done in Swanson-
 Hysell et al. (2019). This approach provides the mean pole position on the apparent po-
 lar wander path. We also wish to report the uncertainty on that estimated position. The
 spread in the position of these inverted pole positions has real meaning related to the
 certainty of the path position at a given time resulting from the Euler pole positions and
 rotation rates in the posterior distribution. The spread in pole positions can be approx-
 imated as a Fisher distribution from which the angle from the mean that contains 95%
 of the solutions (θ_{95}) can be calculated:

$$\theta_{95} = \frac{140^\circ}{\sqrt{\kappa}} \quad (21)$$

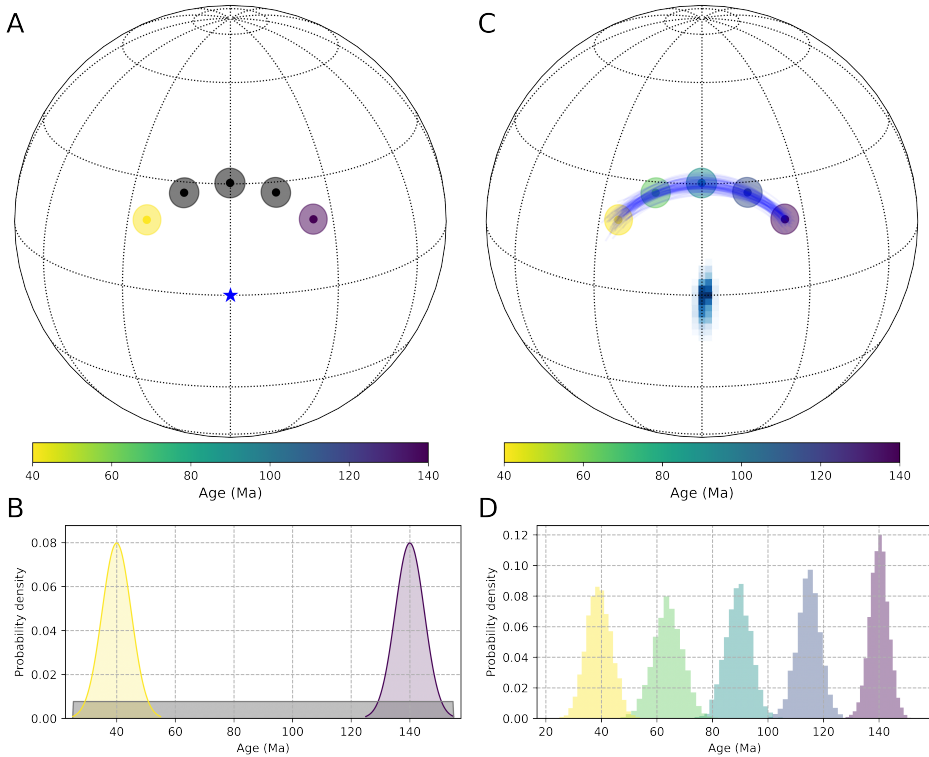


Figure 5. Synthetic data and one Euler pole inversion incorporating age uncertainty. (A, B) Assigned distributions associated with the paleomagnetic pole positions and ages. We take the first and last poles to be radiometrically dated with 1σ uncertainties of 5 Myr such that they are assigned Gaussian prior distributions. The middle three poles are undated and constrained to be between the first and last poles with uniform probability. (C, D) Posterior distributions after 10^4 MCMC samples of the Euler pole position and pole ages. The posterior distributions for the age of the middle three poles are centered on their true values of 115 Ma, 90 Ma, and 65 Ma. The middle poles help constrain the location of the Euler pole, but with their wide uniform prior age distributions do little to constrain the rotation rate.

511 This angle is analogous to a 2σ uncertainty in Gaussian statistics. The pole positions
 512 typically are consistent with being drawn from a Fisher distribution such that reporting
 513 the 95% confidence of angular deviation can be appropriate, but note that the dis-
 514 tributions are not necessarily Fisherian such that this can be a simplified approximation.
 515 Regardless, implied pole positions from these inversions are more tightly clustered than
 516 the inverted Euler pole positions themselves. This approach for summarizing an APWP
 517 is applied to Australia's Cenozoic path in the following section.

518 Application to Australia's Cenozoic APWP

519 Australia and East Antarctica were connected from the Proterozoic Eon until the
 520 Mesozoic Era when rifting led to the onset of seafloor spreading between the continents
 521 ca. 83 Ma (Williams et al., 2011; Veevers, 2012). Australia's plate motion relative to East
 522 Antarctica is considered to be well constrained from ca. 61 Ma to the present on the ba-
 523 sis of fracture zones and magnetic anomaly data (Cande & Stock, 2004). The plate mo-
 524 tion model of Müller et al. (2016) utilizes the reconstruction of Australia relative to East
 525 Antarctica of Cande and Stock (2004) for 38 Ma to the present-day and that of Whittaker
 526 et al. (2007) for 100 to 38 Ma. The absolute motion of Australia is constrained in the
 527 model through a plate circuit that reconstructs Australia relative to East Antarctica, East
 528 Antarctica relative to Africa, and Africa relative to the spin axis (Müller et al., 2016).
 529 The relative motions between the plates in this plate circuit that are implemented in the
 530 plate model of Torsvik and Cocks (2017) have small differences from that of Müller et
 531 al. (2016) such as the use of Tikku and Cande (2000) for the Australia to East Antarc-
 532 tica rotation between 84 and 44 Ma. Despite these small differences, the overall relative
 533 motions are quite similar. A more significant difference is the use of a different reference
 534 frame for the solid Earth relative to spin axis between Müller et al. (2016) and Torsvik
 535 and Cocks (2017). The choice in this regard is important as pertains to comparisons with
 536 paleomagnetic data as paleomagnetic data is in the reference frame of the spin axis. The
 537 model of Müller et al. (2016) reconstructs plates relative to the global moving hotspot
 538 reference frame of Torsvik et al. (2008) which is taken as fixed relative to the spin axis
 539 over the Cenozoic. In contrast, Torsvik and Cocks (2017) utilize the global moving hotspot
 540 reference frame of Doubrovine et al. (2012) which includes true polar wander rotation
 541 between that reference frame and the spin axis. Notably, a recent analysis of interpreted
 542 hotspot tracks in Eastern Australia by Hansma and Tohver (2020) argued that their po-
 543 sition in a paleomagnetic reference frame is consistent with the true polar wander im-
 544 plemented in the Doubrovine et al. (2012) reference frame. In Figure 6, we show the im-
 545 plied pole position for Australia that results from these global plate motion models. Both
 546 models imply faster Euler rotation rates after \sim 35 Ma than before that time associated
 547 with an acceleration in Australia's northward drift (Fig. 6D). We use these plate mo-
 548 tion models that are largely based on seafloor data as a comparison to an inversion of
 549 Cenozoic paleomagnetic data from Australia for the past 60 million years.

550 There is a contentious history of interpreting Australia's Cenozoic paleomagnetic
 551 record leading to varying APWPs with discussions of the relative fidelity of igneous and
 552 sedimentary poles in the literature (e.g. Idnurm, 1985; Musgrave, 1989; Idnurm, 1994;
 553 Hansma & Tohver, 2019). The paleomagnetic pole database for Australia in the Ceno-
 554 zoic has improved substantially with the development of both new Oligocene and Miocene
 555 paleomagnetic data (Hansma & Tohver, 2018, 2019) and Ar-Ar dates that provide ages
 556 for both previously undated units and supersede previous K-Ar dates (Cohen et al., 2008;
 557 Knesel et al., 2008; Cohen et al., 2013). This updated paleomagnetic pole database is
 558 listed in Table 1 and visualized in Figure 6A. These paleomagnetic poles give us the op-
 559 portunity to develop paleomagnetic Euler pole inversions that can be compared to the
 560 independent plate tectonic reconstructions of Müller et al. (2016) and Torsvik and Cocks
 561 (2017).

Study/Region	Rock type	FLat	PLon	A ₉₅	N	Pmag reference	Age (Ma)	Age min	Age max	Age information	Dist type
Holocene lake sediments	sedimentary	89.4	144.6	1.5	57	Idnurm (1985)	0.005	0	0.01	radiocarbon dates from Idnurm (1985)	uniform
Plio-Pleistocene mean	mixed	87.7	353	3.2	48	as in Hansma and Tolver (2019)	2	1	3	as compiled in Hansma and Tolver (2019)	uniform
Glenample Fm./Port Campbell Lst.	sedimentary	77.2	303.5	3.9	30	Idnurm (1985)	13	9	17	biostratigraphy from Dickinson et al. (2002)	uniform
Cosgrove leucite lavas	igneous	80.2	275.4	8.6	15	Hansma and Tolver (2018)	16	15	17	Ar-Ar dates with range assigned by Hansma and Tolver (2018)	uniform
Main Range Volcano	igneous	76.6	271.6	6.1	25	as in Hansma and Tolver (2019)	23.45	20.2	26.7	Ar-Ar dates from Knesel et al. (2008)	uniform
Tweed Volcano	igneous	77.4	306.9	5.4	48	as in Hansma and Tolver (2019)	23.9	23.1	24.7	Ar-Ar dates from Knesel et al. (2008)	uniform
Pt. Addis Limestone	sedimentary	68.5	299.4	4.8	4.8	Idnurm (1985)	25.1	22.4	27.8	Ar-Ar and biostratigraphic constraints from Idnurm (1985); McLaren et al. (2009)	uniform
Springsure Volcano	igneous	70.5	300.6	9.7	18	Hansma and Tolver (2019)	28.1	27.8	28.4	Ar-Ar date from Cohen et al. (2013)	normal
Peak Range	igneous	64.6	291.8	8.8	29	Hansma and Tolver (2019)	29.65	28.2	31.1	Ar-Ar dates from Cohen et al. (2013)	uniform
Hillsborough Volcano	igneous	67.1	301.4	7.1	14	Hansma and Tolver (2019)	33.6	33.1	34.1	Ar-Ar date from Cohen et al. (2013)	normal
Browns Creek Formation	sedimentary	65.5	292.5	2.5	33	Idnurm (1994)	35.5	36.2	34.9	biostratigraphy and magnetostratigraphy from Shafik and Idnurm (1997)	uniform
North Rankin 1 Drill- core	sedimentary	61.7	298.4	5.1	20	Idnurm (1985)	59.75	57	62.5	foraminiferal zones P3 and P4 (ages of 62.5 to 57 in GTS 2020)	uniform

Table 1. Paleomagnetic poles and age constraints used for the Australia Cenozoic APWP inversion and associated references. N = number of site level VGP used to calculate the mean pole positions; Pmag reference = reference for paleomagnetic pole data; Age (Ma) = nominal age calculated from age constraints on paleomagnetic poles; Age min = lower bounds for pole ages; Age max = upper bounds for pole ages; Age information = summary description for geochronology methods for pole ages and associated references; Dist type = choice of using uniform or normal distributions for assigning prior uncertainties for pole ages.

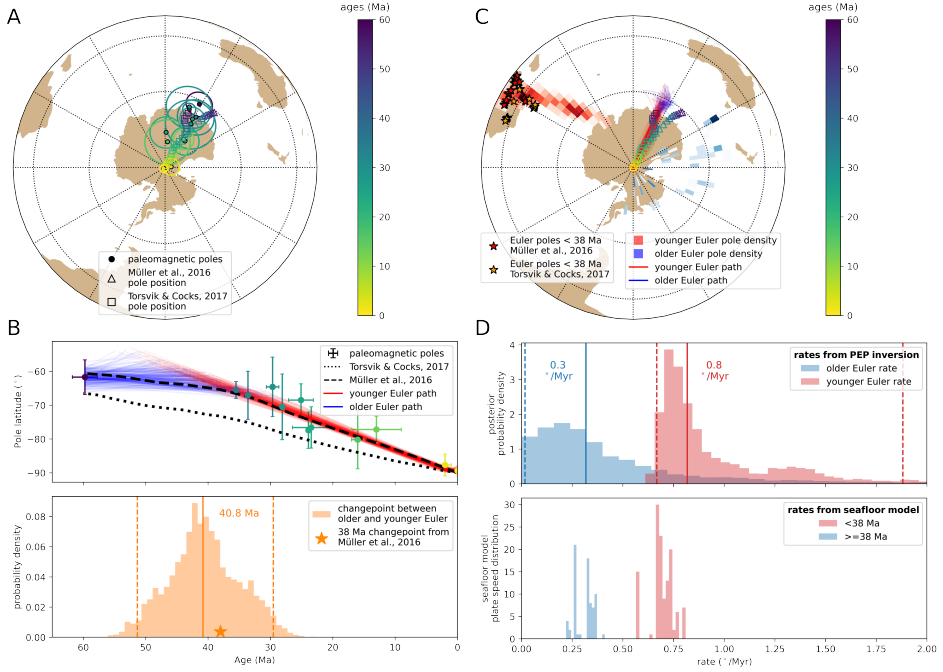


Figure 6. A) Cenozoic paleomagnetic poles for Australia used for the Bayesian inversion model are shown as circles with their A_{95} confidence ellipses colored by age. The continuous path using the same color scale is the implied pole position extracted from the Müller et al. (2016) and Torsvik and Cocks (2017) models which are dominantly based on seafloor data for this time interval. B) The latitude of the pole position for the paleomagnetic poles is shown with their positional and temporal uncertainties. The black lines are the latitude of the pole position implied by the Müller et al. (2016) and Torsvik and Cocks (2017) models which undergo changes in slope ca. 40 to 35 Ma. The thin red and blue lines are 100 of the pole paths resulting from the two Euler pole inversion with blue being the older path segment and red the younger segment. The lower histogram shows the posterior distribution of the age of changepoints from the older to younger Euler pole in the inversion which has a median of 40.8 Ma. C) 100 sample paths (blue older; red younger) from the inversion are shown in comparison to the Müller et al. (2016) (triangles) and Torsvik and Cocks (2017) (squares) paths as well as density of the two inverted Euler poles (blue and red rectangles). Due to the low number of paleomagnetic poles between 60 Ma and the changepoint, as well as the short length of the path, the position of the older Euler pole is not tightly constrained leading to the sparse blue density. The posterior distribution of the younger Euler pole position (red density on the globe) is more tightly constrained and coincides with the Euler poles (red stars) extracted from the global plate reconstruction models. D) The top panel shows the posterior distribution of the Euler rotation rates associated with the older and younger inverted Euler poles with the median shown with the solid line and the labeled rates. The lower panel is the Euler rotation rates for Australia extracted from the Müller et al. (2016) global plate reconstruction model before and after 38 Ma illustrating good correspondence between the median of the inversion posterior and the rates from this seafloor data based model.

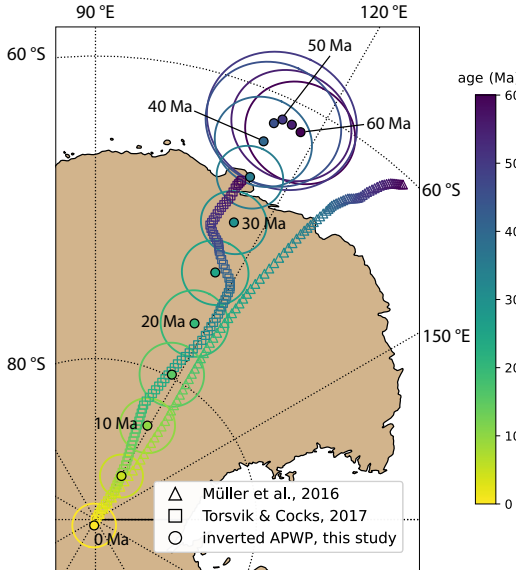


Figure 7. Summary of the apparent polar wander path (APWP) for Australia in the Cenozoic based on a two plate tectonic Euler poles Bayesian inversion to the paleomagnetic poles (Fig. 6). The Fisher angular deviation (θ_{95}) of the positions along the inverted paths are shown in 5 Myr intervals from 60 to 0 Ma (Table 2). Also shown are the pole positions implied by the continuous reconstructions of Müller et al. (2016) and Torsvik and Cocks (2017) which vary in terms of their reference frames as discussed in the text. The new inverted APWP matches better in terms of pole position latitude with the global plate reconstruction model of Müller et al. (2016), but better in terms of pole position longitude with the model of Torsvik and Cocks (2017).

The paleomagnetic data necessitate at least one change in the Euler pole between 60 Ma and the present. This need for more than one Euler pole is most readily visualized in the latitude of the poles which implies a change in rate between 60 Ma and the present (Fig. 6B). We apply the Bayesian inversion framework to invert for two Euler poles for Cenozoic Australia using prior probability constraints from these paleomagnetic poles. We use an uninformed prior probability for the timing of the changepoint between the two Euler poles in which it is assigned a uniform probability distribution between the age of the oldest (~ 60 Ma) and the youngest paleomagnetic poles (~ 0.005 Ma) in the compilation. We also use a weakly informative uniform prior distribution of $U(0, 4)$ for the Euler rotation rate, as we know based on the position and age of the paleomagnetic poles that the overall plate motion rate for Australia in the Cenozoic is most likely to be less than $4^\circ/\text{Myr}$ (Fig. 6A). For the prior distribution for the Euler rotation axes, we use a weakly informative Watson girdle distribution with $\kappa_W = -0.1$.

The posterior distribution of the Euler pole positions, samples of the small circle paths generated from the posterior distributions, the implied pole latitudes, and the full plate motion angular rotation rates are shown in Figure 6. The probability density of the inverted positions for the younger Euler pole (ca. 40 Ma to present) is more tightly constrained than the older Euler pole position given both the higher number of paleomagnetic poles and longer track length. The posterior distribution of the younger Euler pole positions (red density in Fig. 6B) recovered through the inversion correspond well with the Euler pole positions extracted from the Müller et al. (2016) and Torsvik and Cocks (2017) models (red and pink stars in Fig. 6C). The inversion is also successful in recovering the change in rate seen in both models where Australia's plate motion

Table 2. Bayesian paleomagnetic Euler pole apparent polar wander path for Cenozoic Australia

Bayesian PEP (2 plate tectonic Euler poles)			
Age (Ma)	PLon°	PLat°	Θ_{95}
60	117.9	-61.8	3.5
55	116.4	-61.6	3.8
50	115.1	-61.6	4.8
45	114.2	-62.0	4.3
40	114.0	-63.5	3.1
35	114.3	-66.1	2.1
30	115.0	-69.3	2.1
25	115.9	-72.8	2.1
20	116.8	-76.3	2.1
15	117.8	-79.8	2.0
10	118.9	-83.4	1.7
5	120.8	-86.9	1.3
0	282.6	-89.6	1.4

Notes: PEP: paleomagnetic Euler pole; PLon: pole longitude; PLat: pole latitude; Θ_{95} represents the Fisher angular deviation wherein 95% of the estimated path positions lie within that angle of the mean path position assuming a Fisher distribution.

accelerated in the later portion of the Eocene (Fig. 6B). The posterior distributions for Euler rotation rates have median values that increase from $0.3^\circ/\text{Myr}$ to $0.8^\circ/\text{Myr}$ (Fig. 6D). The 95% credible interval for the age of the changepoint associated with this change in rate spans from ca. 51 to 30 Ma with a median 40.8 Ma. While this broad posterior distribution reflects the sparse paleomagnetic poles constraints between 60 and 40 Ma, the timing of the change in rate is consistent with the Müller et al. (2016) and Torsvik and Cocks (2017) models (Fig. 6B).

There is a closer correspondence between the latitude of the path inverted using the paleomagnetic pole constraints with the Müller et al. (2016) model than the Torsvik and Cocks (2017) model as can be seen by the inverted paths (red for younger Euler; blue for older Euler) plotting atop the thicker dashed line in Figure 6B. In contrast, there is a tighter correspondence between the longitude of the pole path resulting from the inversion with the Torsvik and Cocks (2017) model as seen in Figure 6B where the inverted paths are atop the squares which mark the Torsvik and Cocks (2017) path. The path of Müller et al. (2016) deviates to the east from the inverted paths whose trajectory are being constrained by the ca. 60 Ma North Rankin 1 Drillcore pole (Table 1). To facilitate these comparisons, we apply the approach described in the *Reporting the apparent polar wander path* section to summarize the new APWP (Table 2) and plot it with the implied pole positions of the Müller et al. (2016) and Torsvik and Cocks (2017) models in Figure 7.

It is intriguing that the inclusion of the Doubrovine et al. (2012) true polar wander correction in the Torsvik and Cocks (2017) model results in improved correspondence in the terms of pole longitude, but more of a discrepancy with the paleomagnetic poles and their inversion in terms of latitude (Figs. 6 and 7). While the conclusions that can be drawn in this regard are limited given the restriction of the analysis to Australia, such comparisons could be a fruitful future direction to use for comparisons between reference frames. Overall, the analysis highlights a broad agreement in the interpretation of kinematics that results from inversion of the Cenozoic paleomagnetic poles for Australia and that which results from seafloor-based plate motion models.

614 **Application to the Keweenawan Track**

An impetus for the development of this Bayesian paleomagnetic Euler pole inversion method was to constrain the absolute rates of plate motion associated with the ca. 615 1109 to 1070 Ma Keweenawan Track of paleomagnetic poles from the Proterozoic continent of Laurentia (Halls & Pesonen, 1982; Swanson-Hysell et al., 2009, 2019). These 616 poles are associated with the rapid motion of Laurentia towards the equator leading up 617 to the Grenvillian orogeny and the assembly of the supercontinent Rodinia (Swanson- 618 Hysell, 2021). While previous approaches had established estimates for the rate of lat- 619itudinal motion associated with the Keweenawan Track (Davis & Green, 1997; Swanson- 620 Hysell et al., 2014), this Bayesian inversion method was implemented in Swanson-Hysell 621 et al. (2019) in order to constrain absolute rates (without providing the level of detail 622 on the methodology that is elucidated in the present contribution). In addition to our 623 goals of constraining absolute rates, this approach was particularly appropriate for the 624 Keweenawan Track as it includes poles with quite disparate precision on their age con- 625 straints as some are constrained tightly by high-precision U-Pb dates (e.g. Fairchild et 626 al., 2017) while others have looser stratigraphic constraints. A technical note related to 627 the analysis in Swanson-Hysell et al. (2019) is that it used a version of the code writ- 628 ten in PyMC2 (Patil et al. (2010); <https://github.com/ian-r-rose/mcplates>). The 629 PyMC project has migrated to PyMC3 (now known simply as PyMC) which is a total 630 rewrite of the module (Salvatier et al., 2016) and necessitated our code to refactored into 631 its present PyMC version (https://github.com/Swanson-Hysell-Group/Bayesian_PEP_inversion). These two versions of the code apply the same methodology and recover 632 very similar solutions. One change that we adopted in this study is that we applied 633 inclination shallowing corrections to the sedimentary paleomagnetic poles within the Ke- 634 weenawan Track (i.e. the Nonesuch Formation and lower Freda Formation poles of Henry 635 et al. (1977)) given how widespread inclination shallowing is for remanence held by de- 636 trital hematite. While more research is needed on these sedimentary rocks to quantify 637 the degree of inclination shallowing, we take the approach of Domeier et al. (2012) in 638 utilizing an assumed flattening factor of 0.6 given that sample-level data are not avail- 639 able. A ripe direction for future work would be to adopt a probabilistic framework for 640 inclination shallowing correction rather than an assigned single value.

For all Keweenawan Track inversions, we use weakly informative Watson girdle dis- 641 tributions with $\kappa_W = -0.1$ for the prior distribution of Euler poles, and use an expo- 642 nential distribution with $\lambda = 2.5$ for the prior distribution of Euler rotation rates (based on 643 the analysis shown in Figure 3). Paleomagnetic Euler pole inversions to the Keweenawan 644 Track are shown in Figures 8 and 9. The posterior distribution of the Euler pole posi- 645 tions are shown along with a sampling of pole positions generated from the posterior Eu- 646 ler parameters and pole ages which are plotted over the paleomagnetic poles (as com- 647 piled in Swanson-Hysell et al. (2019)). The prior distributions for the ages of the poles 648 are shown in Fig. 9B. The prior probabilities assigned to the ages illustrate the variable 649 age uncertainties associated with the paleomagnetic poles in the Keweenawan Track some 650 of which are tightly constrained by radiometric dates and others which have looser age 651 constraints (Swanson-Hysell et al., 2019). The posterior distribution of the angular 652 rotation rates for Laurentia resulting from the inversions are shown as angular velocities 653 along with their 95% credible intervals (Figs. 8 and 9). To compare models with vary- 654 ing combinations of Euler poles and assess whether the results of the inversions repre- 655 sent good fits for the observed paleomagnetic poles, we calculate the distribution of the 656 natural log of the likelihood for the paleomagnetic poles generated from the posterior 657 Euler parameters and pole ages based on the observed paleomagnetic poles. A summary 658 of the posterior likelihood distributions is shown in Fig. 8B.

Applying a single paleomagnetic Euler pole inversion to the entirety of the Keweenawan 660 Track results in a median rate of $3.1^\circ/\text{Myr}$ with a 95% credible interval of 2.7 to $3.6^\circ/\text{Myr}$ 661 (Fig. 8). In the literature, the Keweenawan Track has variably be interpreted as being 662

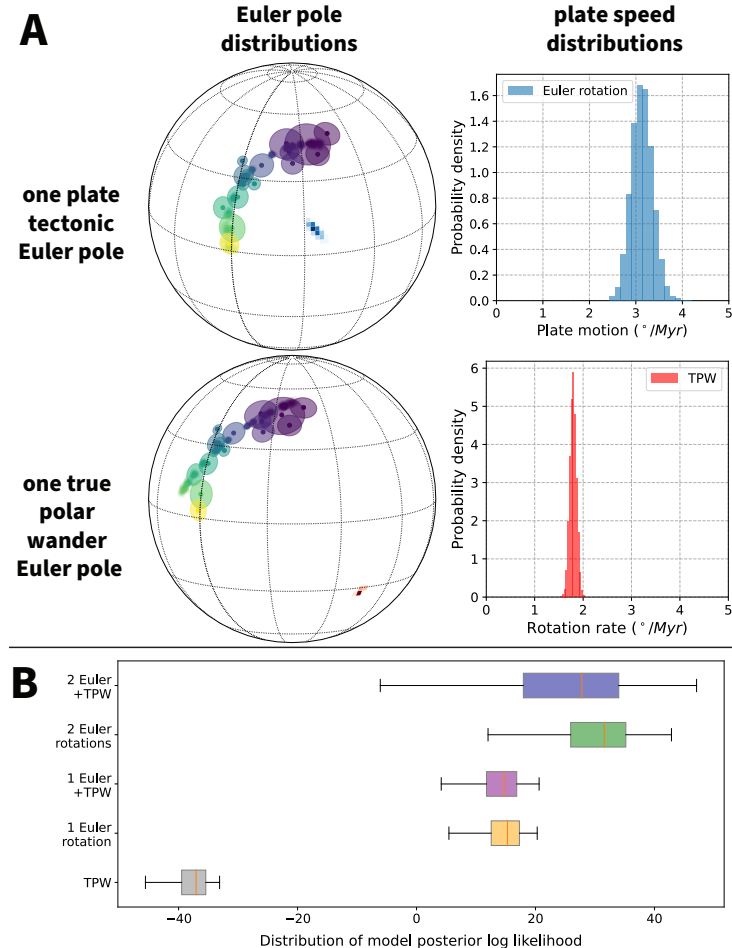


Figure 8. A) Bayesian paleomagnetic Euler pole inversions of the Keweenawan Track for one plate tectonic Euler pole and for one true polar wander Euler pole. The Euler pole locations and representative predicted pole positions associated with posterior Euler parameters and pole ages are shown with the observed paleomagnetic poles on the left orthographic projections. Details on the individual paleomagnetic poles used in the analysis can be found in Swanson-Hysell et al. (2019). The distribution of angular rotation rates resulting from the inversions are shown in the histograms on the right. B) Posterior likelihood distributions for all models used to invert for the Keweenawan Track. The log likelihood values are calculated by taking the natural log of equation 20 and show the true polar wander (TPW) inversion to have a quite low likelihood relative to the other inversions.

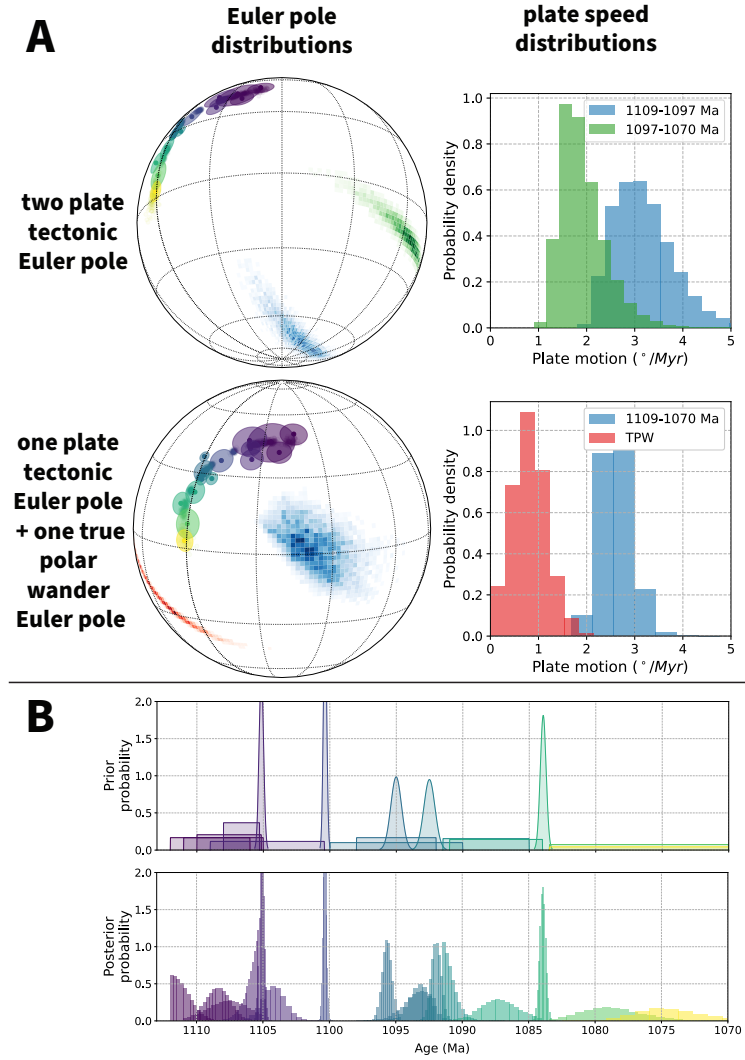


Figure 9. A) Bayesian paleomagnetic Euler pole inversion of the Keweenawan Track for two plate tectonic Euler poles with a change point and for one Euler pole with concurrent true polar wander. The Euler pole locations, representative predicted pole positions, and the distribution of angular rotation rates associated with each model are shown in the same way as in Fig. 8. For the plate tectonic Euler pole, the position (in blue density) is shown relative to the start position of the path. The true polar wander rotation will progressively rotate these plate tectonic Euler poles such that the position will change through time. The log likelihood of these models are compared with others in Fig. 8B. B) Top: prior age distributions for poles used in the forward model. Bottom: posterior pole age distributions resulting from the two plate tectonic Euler pole MCMC inversion.

the result of fast differential plate motion (e.g. Davis & Green, 1997) or as the result of true polar wander (e.g. Evans, 2003). True polar wander results in rotation of the entire silicate Earth about an Euler pole 90° from the path and has the potential to progress at rapid rates (Rose & Buffett, 2017). Overall, true polar wander is a difficult signal to disentangle from plate motions, since any given APWP can be the result of true polar wander, plate tectonics, or some combination of the two. However, given the nature of a true polar wander rotation, an Euler pole that describes true polar wander will be 90° from the spin axis such that the Euler pole for a true polar wander event will be 90° from the paleomagnetic poles. Therefore, the extent to which true polar wander could explain motion of the Keweenawan Track can be evaluated by constraining the location of the true polar wander Euler pole to be within a great circle 90° from the path. This constraint is imposed in the inversion by using a restrictive Watson girdle distribution. As shown in Swanson-Hysell et al. (2019), a single true polar wander rotation is a poor fit to the path given its curvature. The posterior true polar wander rotation parameters results in a path that deviates from the observed paleomagnetic poles, as is illustrated by the resampled poles for younger ages falling outside of the A₉₅ uncertainty ellipses of the observed paleomagnetic poles in Fig. 8A. As a result, the posterior log likelihood values for the true polar wander model are much smaller than those for the one Euler pole model (Fig. 8B).

The pole path could be the result of a combination of true polar wander and differential plate motion. This scenario can be explored through models that invert for a true polar wander Euler pole as well as differential plate tectonic Euler poles. The model with both a plate tectonic Euler pole rotation and a concurrent true polar wander rotation partitions the motion between both with significantly faster plate tectonic motion (Fig. 9A). In addition, because the true polar wander involves the rotation of the solid Earth with respect to the spin axis (rotating both the plate and its associated Euler pole), its results in more uncertainty associated with the location of the plate tectonic Euler pole, broadening the posterior Euler pole distribution (Fig. 9A). Although such a rotation is possible, adding a true polar wander component to either the one or two plate tectonic Euler pole inversions does not significantly improve fits to the observed paleomagnetic poles Figure 8B. Overall, forward models involving small circle Euler rotations always yield better fits to the observed paleomagnetic data than the model that considers only true polar wander great circle rotation (Fig. 8). These results indicate that there was rapid plate motion at the time which is associated with subduction that led to the closure of the Unimor Ocean leading up to collisional Grenvillian orogenesis and the associated formation of the supercontinent Rodinia (Hynes & Rivers, 2010; Swanson-Hysell et al., 2022). In comparison with models that involve one Euler pole rotation, the two Euler pole inversion results in an improvement in fit as can be visualized by the modeled pole positions shown in Figure 9A and by the calculated posterior likelihood distributions for the paleomagnetic pole positions (Fig. 8B). The two Euler pole inversion results in a ca. 1097 Ma changepoint age (with a 95% credible interval from 1098.8 to 1095.4 Ma) with rates that slow from $\sim 3.1^\circ/\text{Myr}$ to $\sim 1.8^\circ/\text{Myr}$ after the changepoint. This change could be associated with initial onset of collisional Grenvillian orogenesis along Laurentia's margin (Swanson-Hysell et al., 2019).

The results of this Bayesian Euler pole inversion method can not only provide insights into geodynamic processes, but also provide geochronologic estimates on rock units that have poor or none radiometric age constraints. As our knowledge of paleomagnetic pole ages and their uncertainties are incorporated into the inversions, the more informative prior distributions that we implement for poles that have well-constrained radiometric dates (such as the normal distributions for many igneous units of the Keweenawan Track) can act as anchor points and result in more tightly constrained posterior distributions for ages of other poles that have less informative priors (such as the uniform distributions for some igneous and the sedimentary poles of the Keweenawan Track). As is illustrated in Figure 9B, the poles whose ages could only be bracketed as uniform dis-

tributions in the prior end up having posterior age distributions with more constrained credible intervals. In this example, these ages estimated through paleomagnetic Euler pole inversion model give insight into the chronology of magmatism and basin development within the North American Midcontinent Rift.

Challenges and opportunities in the application of paleomagnetic Euler pole analysis

While the examples in this study highlight insights that can be gained through applying paleomagnetic Euler pole analysis to segments of apparent polar wander paths, challenges remain in its broad application. One set of challenges relates to the resolving power of the method. For slow rates of motion, the position of inverted Euler poles are uncertain and it is difficult to resolve the timing of changepoints with confidence. However, this issue is more related to the precision of available constraints and is the case regardless of method. Of note is that the spread between resulting paths is much less than the spread of the posterior Euler pole position (as in the older Euler pole rotation in the Australia application; Fig. 6). Determining the number of change points to implement in an inversion is an additional challenge, and one that is also more difficult for slow motions or uncertain data. This issue is addressed theoretically in Gallo et al. (2022) who apply a frequentist approach to paleomagnetic Euler pole inversion and propose a graphical approach to evaluate for the optimal number of inverted Euler poles. The extension of such an approach beyond ideal synthetic data to noisier suites of paleomagnetic data as well as integration with our Bayesian inversion approach could prove fruitful.

It could be interpreted as an advantage of paleomagnetic Euler pole analysis that it utilizes a physical model of plate motions to inform an APWP shape that fits with our knowledge of plate motions. However, uncertainty remains regarding underlying assumptions including that Euler pole positions and associated plate motions are relatively stable over millions of years. A complexity here is that while data constrain the relative motion between plates to be relatively constant (e.g. Müller et al. (2016)), the motion of a plate relative to the spin axis can be the combined effect of multiple Euler poles in a plate circuit as well as true polar wander. Furthermore, the method also assumes that the timescale over which Euler pole positions themselves migrate are relatively rapid such that they can be approximated by instantaneous changepoints. Evaluating the validity of these assumptions is an area ripe for future research. There is the potential to apply paleomagnetic Euler pole inversion itself to gain insight into these uncertainties.

An additional opportunity comes from the method giving posterior distributions for pole ages. There is a long history of paleomagnetists comparing undated (or poorly dated) paleomagnetic poles with APWPs to gain insight on their age (McCabe et al., 1984; Hnatyshin & Kravchinsky, 2014). These methods typically rely on comparison between designated pole pairs or consider the reference APWP to not have uncertainty. In the Bayesian paleomagnetic Euler pole inversion method developed here, undated poles (Fig. 5) or poorly dated (Fig. 9) poles can be incorporated into the analysis with the resulting posterior distribution age distribution providing an estimate of the age of magnetization including uncertainty.

Conclusions

We have extended the paleomagnetic Euler pole analysis of Gordon et al. (1984) by placing it within a Bayesian framework. As a Bayesian inverse problem, Markov chain Monte Carlo (MCMC) numerical methods can be used to obtain estimates of Euler pole positions and rates as constrained by paleomagnetic poles. Regularization of the inversions is not accomplished by smoothing parameters, but can instead be accomplished through prior probability distributions for the Euler pole parameters, which have clear physical

771 interpretations. The approach enables uncertainties on both the positions and ages of
772 paleomagnetic poles to be incorporated into the analysis. Multiple Euler poles can be
773 included with the timing of changepoints between them being solved as part of the in-
774 version. An advantage of this approach is that the paleomagnetic Euler poles provide
775 an estimate for the total plate velocity including both latitudinal and relative longitu-
776 dinal motion. The resulting posterior distributions from the inversions provide uncer-
777 tainties for the model parameters – including estimates of plate velocity.

778 Open Research

779 The code implementing the analysis and developing the visualizations of this study
780 are documented within Jupyter notebooks (Kluyver et al., 2016) that are available on
781 Github (https://github.com/Swanson-Hysell-Group/Bayesian_PEP_inversion) and
782 Zenodo (<https://doi.org/10.5281/zenodo.7087844>). These notebooks utilize the func-
783 tions within the bayesian_pep library within the repository and data that are within the
784 repository as well. The computational environment used for running these notebooks and
785 conducting the analysis can be reproduced using the environment.yml file within the repos-
786 itory. Instructions associated with recreating this computational environment can be found
787 in the README.md file within the repository. MCMC analysis was performed using PyMC
788 (Salvatier et al., 2016). Additional analysis was performed using the Python packages
789 NumPy (Harris et al., 2020), Scipy (Virtanen et al., 2020), and PmagPy (Tauxe et al.,
790 2016). Figures were created using Matplotlib (Hunter, 2007) and Cartopy (Met Office,
791 2010 - 2015).

792 Acknowledgments

793 This work was supported by National Science Foundation grants EAR-1246670 and EAR-
794 1847277. We thank Bruce Buffett, David Evans, and Mike Tetley for useful discussions
795 during development of the method. We thank Mat Domeier, Facu Sapienza, Leandro Gallo,
796 and other members of the CEED YC2.0 workshop for informative discussions during the
797 writing of the manuscript. These interactions were supported by a grant from the Peder
798 Sather Center for Advanced Study. We also acknowledge Bram Vaes for an insightful
799 review that improved the manuscript as well as the useful comments of an anonymous
800 reviewer.

801 **References**

- 802 Argus, D. F., Gordon, R. G., & DeMets, C. (2011). Geologically current motion
803 of 56 plates relative to the no-net-rotation reference frame. *Geochemistry, Geo-*
804 *physics, and Geosystems*, 12(11). doi: 10.1029/2011gc003751
- 805 Aster, R. C., Borchers, B., & Thurber, C. H. (2005). *Parameter estimation and in-*
806 *verse problems*. Elsevier.
- 807 Beck, M. E. (1989). Chapter 22: Paleomagnetism of continental North America;
808 Implications for displacement of crustal blocks within the Western Cordillera,
809 Baja California to British Columbia. In L. C. Pakiser & W. D. Mooney (Eds.),
810 *Geophysical Framework of the Continental United States* (Vol. 172). Geological
811 Society of America. doi: 10.1130/MEM172-p471
- 812 Beck, M. E., & Housen, B. A. (2003). Absolute velocity of North America during
813 the Mesozoic from paleomagnetic data. *Tectonophysics*, 377(1-2), 33–54. doi:
814 10.1016/j.tecto.2003.08.018
- 815 Boyden, J. A., Müller, R. D., Gurnis, M., Torsvik, T. H., Clark, J. A., Turner, M.,
816 ... Cannon, J. S. (2011). Next-generation plate-tectonic reconstructions
817 using GPlates. In C. Baru & G. R. Keller (Eds.), *Geoinformatics: Cyberin-*
818 *frastructure for the Solid Earth Sciences* (p. 95-114). Cambridge: Cambridge
819 University Press. doi: 10.1017/CBO9780511976308.008
- 820 Bryan, P., & Gordon, R. G. (1986). Rotation of the Colorado Plateau: An
821 analysis of paleomagnetic data. *Tectonics*, 5(4), 661–667. doi: 10.1029/
822 tc005i004p00661
- 823 Bull, A. L., Domeier, M., & Torsvik, T. H. (2014). The effect of plate motion his-
824 tory on the longevity of deep mantle heterogeneities. *Earth and Planetary Sci-*
825 *ence Letters*, 401, 172–182. doi: 10.1016/j.epsl.2014.06.008
- 826 Butler, R. (1992). *Paleomagnetism: Magnetic domains to geologic terranes*. Black-
827 well Scientific Publications.
- 828 Cande, S. C., & Stock, J. M. (2004). Cenozoic reconstructions of the Australia-New
829 Zealand-South Pacific sector of Antarctica. In *The Cenozoic Southern Ocean:*
830 *Tectonics, sedimentation, and climate change between Australia and Antarctica*
831 (pp. 5–17). American Geophysical Union. doi: 10.1029/151gm02
- 832 Carpenter, B., Gelman, A., Hoffman, M. D., Lee, D., Goodrich, B., Betancourt, M.,
833 ... Riddell, A. (2017). Stan: A probabilistic programming language. *Journal*
834 *of Statistical Software*, 76(1), 1 - 32. doi: 10.18637/jss.v076.i01
- 835 Cohen, B. E., Knesel, K. M., Vasconcelos, P. M., & Schellart, W. P. (2013).
836 Tracking the Australian plate motion through the Cenozoic: Constraints
837 from $^{40}\text{Ar}/^{39}\text{Ar}$ geochronology. *Tectonics*, 32(5), 1371–1383. doi:
838 10.1002/tect.20084
- 839 Cohen, B. E., Knesel, K. M., Vasconcelos, P. M., Thiede, D. S., & Hergt, J. M.
840 (2008). $^{40}\text{Ar}/^{39}\text{Ar}$ constraints on the timing and origin of Miocene leucite
841 volcanism in southeastern Australia. *Australian Journal of Earth Sciences*,
842 55(3), 407–418. doi: 10.1080/08120090701769514
- 843 Cox, A., & Hart, R. (2009). *Plate tectonics: How it works*. Wiley.
- 844 Creveling, J. R., Mitrovica, J. X., Chan, N. H., Latychev, K., & Matsuyama, I.
845 (2012, 11). Mechanisms for oscillatory true polar wander. *Nature*, 491(7423),
846 244–248. doi: 10.1038/nature11571
- 847 Davidson-Pilon, C. (2015). *Bayesian methods for hackers: Probabilistic programming*
848 *and Bayesian inference*. Addison-Wesley.
- 849 Davis, D., & Green, J. (1997). Geochronology of the North American Midcontinent
850 rift in western Lake Superior and implications for its geodynamic evolution.
851 *Canadian Journal of Earth Science*, 34, 476-488. doi: 10.1139/e17-039
- 852 DeMets, C., Gordon, R. G., & Argus, D. F. (2010). Geologically current plate mo-
853 tions. *Geophysical Journal International*, 181(1), 1–80. doi: 10.1111/j.1365
854 -246x.2009.04491.x

- Dickinson, J. A., Wallace, M. W., Holdgate, G. R., Gallagher, S. J., & Thomas, L. (2002, 03). Origin and timing of the Miocene-Pliocene Unconformity in southeast Australia. *Journal of Sedimentary Research*, 72(2), 288–303. doi: 10.1306/082701720288
- Domeier, M., Van der Voo, R., & Torsvik, T. H. (2012, 1). Paleomagnetism and Pangea: The road to reconciliation. *Tectonophysics*, 514–517, 14–43. doi: 10.1016/j.tecto.2011.10.021
- Doubrovine, P. V., Steinberger, B., & Torsvik, T. H. (2012). Absolute plate motions in a reference frame defined by moving hot spots in the Pacific, Atlantic, and Indian oceans. *Journal of Geophysical Research: Solid Earth*, 117(B9). doi: 10.1029/2011JB009072
- Evans, D. A. D. (2003). True polar wander and supercontinents. *Tectonophysics*, 362, 303–320. doi: 10.1016/S0040-1951(02)000642-X
- Fairchild, L. M., Swanson-Hysell, N. L., Ramezani, J., Sprain, C. J., & Bowring, S. A. (2017). The end of Midcontinent Rift magmatism and the paleogeography of Laurentia. *Lithosphere*, 9(1), 117–133. doi: 10.1130/L580.1
- Fisher, N. I., Lewis, T., & Embleton, B. J. J. (1987). *Statistical analysis of spherical data*. Cambridge University Press. doi: 10.1017/CBO9780511623059
- Forsyth, D., & Uyeda, S. (1975). On the relative importance of the driving forces of plate motion. *Geophysical Journal International*, 43(1), 163–200. doi: 10.1111/j.1365-246X.1975.tb00631.x
- Forte, A. M., & Peltier, W. R. (1987). Plate tectonics and aspherical earth structure: The importance of poloidal-toroidal coupling. *Journal of Geophysical Research: Solid Earth*, 92(B5), 3645. doi: 10.1029/jb092ib05p03645
- Francheteau, J., & Sclater, J. G. (1969). Paleomagnetism of the southern continents and plate tectonics. *Earth and Planetary Science Letters*, 6(2), 93–106. doi: 10.1016/0012-821X(69)90126-5
- Gable, C. W., O'Connell, R. J., & Travis, B. J. (1991). Convection in three dimensions with surface plates: Generation of toroidal flow. *Journal of Geophysical Research: Solid Earth*, 96(B5), 8391. doi: 10.1029/90jb02743
- Gallo, L. C., Sapienza, F., & Domeier, M. (2022). An optimization method for paleomagnetic Euler pole analysis. *Computers & Geosciences*, 166, 105150. doi: 10.1016/j.cageo.2022.105150
- Gelman, A., Carlin, J. B., Stern, H. S., & Rubin, D. B. (2013). *Bayesian data analysis*. Chapman and Hall.
- Gelman, A., & Rubin, D. B. (1996). Markov chain Monte Carlo methods in biostatistics. *Statistical Methods in Medical Research*, 5(4), 339–355. doi: 10.1177/096228029600500402
- Goldstein, H. (1965). *Classical mechanics*. Pearson.
- Gordon, R. G., Cox, A., & Harter, C. E. (1978). Absolute motion of an individual plate estimated from its ridge and trench boundaries. *Nature*, 274(5673), 752–755. doi: 10.1038/274752a0
- Gordon, R. G., Cox, A., & O'Hare, S. (1984). Paleomagnetic Euler poles and the apparent polar wander and absolute motion of North America since the Carboniferous. *Tectonics*, 3(5), 499–537. doi: 10.1029/TC003i005p00499
- Halls, H., & Pesonen, L. (1982). Paleomagnetism of Keweenawan rocks. *Geological Society of America Memoirs*, 156, 173–201. doi: 10.1130/MEM156-p173
- Hansma, J., & Tohver, E. (2018). Palaeomagnetism of mid-Miocene leucitite volcanics in eastern Australia. *Geophysical Journal International*, 215(1), 303–313. doi: 10.1093/gji/ggy281
- Hansma, J., & Tohver, E. (2019). Paleomagnetism of Oligocene hot spot volcanics in central Queensland, Australia. *Journal of Geophysical Research: Solid Earth*, 124(7), 6280–6296. doi: 10.1029/2019jb017639
- Hansma, J., & Tohver, E. (2020). Southward drift of eastern Australian hotspots in the paleomagnetic reference frame is consistent with global true polar wander

- estimates. *Frontiers in Earth Science*, 8. doi: 10.3389/feart.2020.544496
- Harris, C. R., Millman, K. J., van der Walt, S. J., Gommers, R., Virtanen, P., Cournapeau, D., ... Oliphant, T. E. (2020). Array programming with Numpy. *Nature*, 585(7825), 357–362. doi: 10.1038/s41586-020-2649-2
- Henry, S. G., Mauk, F. J., & Van der Voo, R. (1977). Paleomagnetism of the upper Keweenawan sediments: Nonesuch Shale and Freda Sandstone. *Canadian Journal of Earth Science*, 14, 1128–1138. doi: 10.1139/e77-103
- Hnatyshin, D., & Kravchinsky, V. A. (2014). Paleomagnetic dating: Methods, MATLAB software, example. *Tectonophysics*, 630, 103–112. doi: 10.1016/j.tecto.2014.05.013
- Hunter, J. D. (2007). Matplotlib: A 2D graphics environment. *Computing in Science & Engineering*, 9(3), 90–95. doi: 10.1109/MCSE.2007.55
- Hynes, A., & Rivers, T. (2010). Protracted continental collision — evidence from the Grenville Orogen. *Canadian Journal of Earth Sciences*, 47(5), 591–620. doi: 10.1139/e10-003
- Iaffaldano, G., Bodin, T., & Sambridge, M. (2012). Reconstructing plate-motion changes in the presence of finite-rotations noise. *Nature Communications*, 3, 1048. doi: 10.1038/ncomms2051
- Idnurm, M. (1985). Late Mesozoic and Cenozoic palaeomagnetism of Australia – I. A redetermined apparent polar wander path. *Geophysical Journal International*, 83(2), 399–418. doi: 10.1111/j.1365-246x.1985.tb06494.x
- Idnurm, M. (1994). New late Eocene pole for Australia, time-averaging of remanence directions, and palaeogeographic reference systems. *Geophysical Journal International*, 117(3), 827–833. doi: 10.1111/j.1365-246x.1994.tb02473.x
- Irving, E. (1977). Drift of the major continental blocks since the Devonian. *Nature*, 270(5635), 304–309. doi: 10.1038/270304a0
- Irving, E., & Park, J. K. (1972). Hairpins and superintervals. *Canadian Journal of Earth Sciences*, 9(10), 1318–1324. doi: 10.1139/e72-115
- Jupp, P. E., & Kent, J. T. (1987). Fitting smooth paths to spherical data. *Journal of the Royal Statistical Society. Series C (Applied Statistics)*, 36(1), 34–46. doi: 10.2307/2347843
- Kluyver, T., Ragan-Kelley, B., Pérez, F., Granger, B., Bussonnier, M., Frederic, J., ... Ivanov, P. (2016). Jupyter notebooks – a publishing format for reproducible computational workflows. In *Positioning and power in academic publishing: Players, agents and agendas*. IOS Press. doi: 10.3233/978-1-61499-649-1-87
- Knesel, K. M., Cohen, B. E., Vasconcelos, P. M., & Thiede, D. S. (2008). Rapid change in drift of the Australian plate records collision with Ontong Java plateau. *Nature*, 454(7205), 754–757. doi: 10.1038/nature07138
- Lunn, D. J., Thomas, A., Best, N., & Spiegelhalter, D. (2000). WinBUGS - A Bayesian modelling framework: Concepts, structure, and extensibility. *Statistics and Computing*, 10(4), 325–337. doi: 10.1023/A:1008929526011
- McCabe, C., der Voo, R. V., & Ballard, M. M. (1984). Late Paleozoic remagnetization of the Trenton Limestone. *Geophysical Research Letters*, 11(10), 979–982. doi: 10.1029/gl011i010p00979
- McLaren, S., Sandiford, M., Dunlap, W. J., Scrimgeour, I., Close, D., & Edgoose, C. (2009). Distribution of Palaeozoic reworking in the Western Arunta Region and northwestern Amadeus Basin from $^{40}\text{Ar}/^{39}\text{Ar}$ thermochronology: implications for the evolution of intracratonic basins. *Basin Research*, 21(3), 315–334.
- McNamara, A. K., & Zhong, S. (2005). Thermochemical structures beneath Africa and the Pacific Ocean. *Nature*, 437(7062), 1136–1139. doi: 10.1038/nature04066
- Met Office. (2010 - 2015). Cartopy: a cartographic python library with a matplotlib interface [Computer software manual]. Exeter, Devon. Retrieved from <http://>

- 965 scitools.org.uk/cartopy
- 966 Minson, S. E., Simons, M., & Beck, J. L. (2013). Bayesian inversion for finite fault
967 earthquake source models I—theory and algorithm. *Geophysical Journal International*, 194(3), 1701–1726. doi: 10.1093/gji/ggt180
- 968 Muller, R., Royer, J.-Y., & Lawver, L. (1993). Revised plate motions relative to
969 the hotspots from combined Atlantic and Indian Ocean hotspot tracks. *Geology*, 21, 275–278. doi: 10.1130/0091-7613(1993)021<0275:RPMRTT>2.3.CO;2
- 970 Müller, R. D., Seton, M., Zahirovic, S., Williams, S. E., Matthews, K. J., Wright,
971 N. M., ... et al. (2016). Ocean basin evolution and global-scale plate reorga-
972 nization events since Pangea breakup. *Annual Review of Earth and Planetary
973 Sciences*, 44(1), 107–138. doi: 10.1146/annurev-earth-060115-012211
- 974 Musgrave, R. J. (1989). A weighted least-squares fit of the Australian apparent
975 polar wander path for the last 100 Myr. *Geophysical Journal International*,
976 96(2), 231–243. doi: 10.1111/j.1365-246x.1989.tb04447.x
- 977 Patil, A., Huard, D., & Fonnesbeck, C. J. (2010). PyMC: Bayesian stochastic mod-
978 elling in Python. *Journal of Statistical Software*, 35(4), 1–81. Retrieved from
979 <https://www.ncbi.nlm.nih.gov/pmc/articles/PMC3097064/>
- 980 Richardson, R. M. (1992). Ridge forces, absolute plate motions, and the intraplate
981 stress field. *Journal of Geophysical Research: Solid Earth*, 97(B8), 11739. doi:
982 10.1029/91jb00475
- 983 Rose, I., & Buffett, B. (2017). Scaling rates of true polar wander in convecting plan-
984 etes and moons. *Physics of the Earth and Planetary Interiors*. doi: 10.1016/j.
985 .pepi.2017.10.003
- 986 Salvatier, J., Wiecki, T. V., Fonnesbeck, C., & Elkan, C. (2016). Probabilistic pro-
987 gramming in Python using PyMC3. *PeerJ Computer Science*, 2, e55. doi: 10
988 .7717/peerj-cs.55
- 989 Cambridge, M., Bodin, T., Gallagher, K., & Tkalčić, H. (2013). Transdimensional
990 inference in the geosciences. *Philosophical Transactions of the Royal Soci-
991 ety A: Mathematical, Physical and Engineering Sciences*, 371(1984). doi:
992 10.1098/rsta.2011.0547
- 993 Seton, M., Müller, R. D., Zahirovic, S., Gaina, C., Torsvik, T., Shephard, G.,
994 ... Chandler, M. (2012). Global continental and ocean basin recon-
995 structions since 200 Ma. *Earth-Science Reviews*, 113(3–4), 212–270. doi:
996 10.1016/j.earscirev.2012.03.002
- 997 Shafik, S., & Idnurm, M. (1997). Calcareous microplankton and polarity rever-
998 sal stratigraphies of the upper Eocene browns creek clay in the Otway Basin,
999 southeast Australia: Matching the evidence. *Australian Journal of Earth
1000 Sciences*, 44(1), 77–86. doi: 10.1080/08120099708728295
- 1001 Sivia, D., & Skilling, J. (2006). *Data analysis: A bayesian tutorial*. Oxford Univer-
1002 sity Press.
- 1003 Smirnov, A. V., & Tarduno, J. A. (2010). Co-location of eruption sites of the
1004 Siberian Traps and North Atlantic Igneous Province: Implications for the na-
1005 ture of hotspots and mantle plumes. *Earth and Planetary Science Letters*,
1006 297(3), 687–690. doi: 10.1016/j.epsl.2010.07.023
- 1007 Swanson-Hysell, N. L. (2021). The Precambrian Paleogeography of Laurentia. In
1008 L. J. Pesonen, D. A. D. Evans, S. Å. Elming, J. M. Salminen, & T. Veikko-
1009 lainen (Eds.), *Ancient Supercontinents and the Paleogeography of the Earth*
1010 (p. 109-153). Elsevier. doi: 10.1016/B978-0-12-818533-9.00009-6
- 1011 Swanson-Hysell, N. L., Maloof, A. C., Weiss, B. P., & Evans, D. A. D. (2009).
1012 No asymmetry in geomagnetic reversals recorded by 1.1-billion-year-old Ke-
1013 weenawan basalts. *Nature Geoscience*, 2, 713–717. doi: 10.1038/ngeo622
- 1014 Swanson-Hysell, N. L., Ramezani, J., Fairchild, L. M., & Rose, I. R. (2019). Failed
1015 rifting and fast drifting: Midcontinent Rift development, Laurentia’s rapid
1016 motion and the driver of Grenvillian orogenesis. *GSA Bulletin*, 131, 913–940.
1017 doi: 10.1130/b31944.1
- 1018
- 1019

- 1020 Swanson-Hysell, N. L., Rivers, T., & van der Lee, S. (2022). The late Mesoproterozoic to early Neoproterozoic Grenvillian Orogeny and the assembly of Rodinia: Turning point in the tectonic evolution of Laurentia. In S. Whitmeyer, D. Kelllett, B. Tikoff, & M. Williams (Eds.), *Laurentia: Evolution of a continent*. Geological Society of America Memoir. doi: 10.1130/2022.1220(14)
- 1021
1022
1023
1024
1025 Swanson-Hysell, N. L., Vaughan, A. A., Mustain, M. R., & Asp, K. E. (2014). Confirmation of progressive plate motion during the Midcontinent Rift's early magmatic stage from the Osler Volcanic Group, Ontario, Canada. *Geochemistry Geophysics Geosystems*, 15, 2039–2047. doi: 10.1002/2013GC005180
- 1026
1027
1028 Tarduno, J. A., McWilliams, M., & Sleep, N. (1990). Fast instantaneous oceanic plate velocities recorded by the Cretaceous Laytonville limestone: Paleomagnetic analysis and kinematic implications. *Journal of Geophysical Research-Solid Earth*, 95(B10), 15503. doi: 10.1029/jb095ib10p15503
- 1029
1030
1031 Tarling, D. H., & Abdeldayem, A. L. (1996). Palaeomagnetic-pole errors and a 'small-circle' assessment of the Gondwanan polar-wander path. *Geophysical Journal International*, 125(1), 115–122. doi: 10.1111/j.1365-246X.1996.tb06538.x
- 1032
1033
1034 Tauxe, L. (2010). *Essentials of paleomagnetism*. University of California Press.
- 1035 Tauxe, L., Shaar, R., Jonestrask, L., Swanson-Hysell, N., Minnett, R., Koppers, A., ... Fairchild, L. (2016). PmagPy: Software package for paleomagnetic data analysis and a bridge to the Magnetics Information Consortium (MagIC) Database. *Geochemistry, Geophysics, Geosystems*, 17, 2450-2463. doi: 10.1002/2016GC006307
- 1036
1037
1038 Tikkoo, A. A., & Cande, S. C. (2000). On the fit of Broken Ridge and Kerguelen plateau. *Earth and Planetary Science Letters*, 180(1-2), 117–132. doi: 10.1016/s0012-821x(00)00157-6
- 1039
1040
1041 Torsvik, T. H., & Cocks, L. R. M. (2017). *Earth history and palaeogeography*. Cambridge University Press. doi: 10.1017/9781316225523
- 1042 Torsvik, T. H., Müller, R. D., Van der Voo, R., Steinberger, B., & Gaina, C. (2008). Global plate motion frames: Toward a unified model. *Reviews of Geophysics*, 46(3), RG3004. doi: 10.1029/2007RG000227
- 1043 Torsvik, T. H., Smethurst, M. A., Meert, J. G., Van der Voo, R., McKerrow, W. S., Brasier, M. D., ... Walderhaug, H. J. (1996). Continental break-up and collision in the Neoproterozoic and Paleozoic – A tale of Baltica and Laurentia. *Earth-Science Reviews*, 40, 229-258. doi: 10.1016/0012-8252(96)00008-6
- 1044 Torsvik, T. H., Smethurst, M. A., Van der Voo, R., Trench, A., Abrahamsen, N., & Halvorsen, E. (1992). Baltica. A synopsis of Vendian-Permian palaeomagnetic data and their palaeotectonic implications. *Earth-Science Reviews*, 33(2), 133–152. doi: 10.1016/0012-8252(92)90023-M
- 1045 Torsvik, T. H., Van der Voo, R., Preeden, U., Mac Niocaill, C., Steinberger, B., Doubrovine, P. V., ... Cocks, L. R. M. (2012). Phanerozoic polar wander, palaeogeography and dynamics. *Earth-Science Reviews*, 114(3-4), 325–368. doi: 10.1016/j.earscirev.2012.06.007
- 1046 Vaes, B., Gallo, L. C., & Hinsbergen, D. J. J. (2022). On pole position: Causes of dispersion of the paleomagnetic poles behind apparent polar wander paths. *Journal of Geophysical Research: Solid Earth*, 127(4). doi: 10.1029/2022jb023953
- 1047 Van der Voo, R. (1990). The reliability of paleomagnetic data. *Tectonophysics*, 184(1), 1–9. doi: 10.1016/0040-1951(90)90116-P
- 1048 Van der Voo, R., & Torsvik, T. (2001). Evidence for late Paleozoic and Mesozoic non-dipole fields provides an explanation for the Pangea reconstruction problems. *Earth and Planetary Science Letters*, 187, 71-81. doi: 10.1016/S0012-821X(01)00285-0
- 1049 Veevers, J. (2012). Reconstructions before rifting and drifting reveal the geological connections between Antarctica and its conjugates in Gondwanaland. *Earth-*
- 1050
1051
1052
1053
1054
1055
1056
1057
1058
1059
1060
1061
1062
1063
1064
1065
1066
1067
1068
1069
1070
1071
1072
1073
1074

- 1075 *Science Reviews*, 111(3-4), 249–318. doi: 10.1016/j.earscirev.2011.11.009
- 1076 Virtanen, P., Gommers, R., Oliphant, T. E., Haberland, M., Reddy, T., Cournapeau,
1077 D., ... SciPy 1.0 Contributors (2020). SciPy 1.0: Fundamental Algorithms
1078 for Scientific Computing in Python. *Nature Methods*, 17, 261–272. doi:
1079 10.1038/s41592-019-0686-2
- 1080 Whittaker, J. M., Müller, R. D., Leitchenkov, G., Stagg, H., Sdrolias, M., Gaina,
1081 C., & Goncharov, A. (2007). Major Australian-Antarctic plate reorgani-
1082 zation at Hawaiian-Emperor bend time. *Science*, 318(5847), 83–86. doi:
1083 10.1126/science.1143769
- 1084 Williams, S. E., Whittaker, J. M., & Müller, R. D. (2011). Full-fit, palinspastic re-
1085 construction of the conjugate Australian-Antarctic margins. *Tectonics*, 30(6).
1086 Retrieved from <https://doi.org/10.1029/2011tc002912> doi: 10.1029/
1087 2011tc002912
- 1088 Zahirovic, S., Müller, R. D., Seton, M., & Flament, N. (2015). Tectonic speed lim-
1089 its from plate kinematic reconstructions. *Earth and Planetary Science Letters*,
1090 418(0), 40–52. doi: 10.1016/j.epsl.2015.02.037